environments

MDPI

Article

Geological and Hydrogeological Controls on Liquefaction Susceptibility in Deltaic Environments: Insights from the Po Delta, Northern Italy

Dimitra Rapti [1,2,*], George Papathanassiou [3], Maria Taftsoglou [4] and Riccardo Caputo [2,4]

[1] Department of Chemical, Pharmaceutical and Agricultural Sciences, Ferrara University, 44122 Ferrara, Italy
[2] New Energies and Environment—NEA Ltd., Ferrara University Spin-Off, 44121 Ferrara, Italy
[3] School of Geology, Aristotle University of Thessaloniki, Egnatia Str., 54124 Thessaloniki, Greece
[4] Department of Physics and Earth Sciences, Ferrara University, 44121 Ferrara, Italy
* Correspondence: dimitra.rapti@unife.it

Abstract

Liquefaction phenomena are strongly influenced by the depositional evolution of the area, including sediment grain size, depositional age, shallow layering, and groundwater depth. This study focuses on a 560 km^2 wide sector of the eastern Po River Plain (northern Italy), encompassing part of the modern Po Delta, to evaluate the susceptibility of the different geological units to liquefaction. A comprehensive dataset was compiled, integrating lithological, chronological (^{14}C), geomorphological, hydrological, and hydrogeological information, together with satellite imagery, historical and modern maps, archaeological evidence, and subsurface data from core drilling and CPTu tests. The integrated analysis allowed us to reconstruct a liquefaction susceptibility map recognizing four classes: very high (4% of the investigated area), high (26%), moderate (20%), and non-susceptible (50%). CPTu-based statistical analyses confirm that the Liquefaction Potential Index (*LPI*) increases with higher susceptibility classes and decreases with increasing groundwater depth (0.5, 1.5, and 3.0 m scenarios). These results provide a scientific basis to support sustainable land management and governance strategies in the Po Delta, an area of high environmental, cultural, and economic value, a large sector of which is included in the Natura 2000 network.

Keywords: geomorphology; hydrogeology; liquefaction hazard; surface geology

Check for updates

Academic Editors: Victor Cavaleiro and Wen-Tien Tsai

Received: 11 May 2026
Revised: 8 June 2026
Accepted: 12 June 2026
Published: 17 June 2026

Copyright: © 2026 by the authors. Licensee MDPI, Basel, Switzerland. This article is an open access article distributed under the terms and conditions of the Creative Commons Attribution (CC BY) license.

1. Introduction

Soil liquefaction represents one of the most significant seismic-induced hazards, as it can lead to loss of soil strength, ground deformation, and widespread structural damage. This natural phenomenon is relatively complex, potentially hazardous and it can generate an impact across multiple temporal and spatial scales (e.g., [1–7]).

In the short term, it may cause (a) devastating effects on the built environment, including the failure or compromise of the structural integrity of building foundations and linear infrastructures, such as roads, power lines, natural gas pipelines, water supply and wastewater systems, as well as irrigation and land reclamation channels; (b) serious threats to artistic and cultural heritage, particularly in urban areas with high historical value; and (c) even the loss of human life.

In the medium to long term, the indirect effects of liquefaction can be equally severe. Economic losses can be substantial, arising not only from reconstruction costs, but also from

the interruption of productive activities, depreciation of property values, and the reduced functionality of critical infrastructures. Furthermore, the consequences for public health and societal well-being can persist over time, through increased psychological stress among the affected population, deterioration of sanitary conditions, and the social vulnerability of communities forced to evacuate or live for extended periods in precarious conditions.

The severity of these impacts has been documented in numerous earthquake events worldwide. For instance, liquefaction associated with the 1989 Loma Prieta earthquake resulted in economic losses estimated at USD 99.2 million [8]. During the 1995 Great Hanshin earthquake, liquefaction and lateral spreading caused extensive damage to port facilities at Kobe, leading to prolonged operational downtime and substantial business interruption costs that affected regional and international trade [9]). Similarly, the 2001 Nisqually earthquake (USA) produced extensive ground deformation and pavement cracking at King County International Airport, resulting in repair and upgrade costs of approximately USD 4.4 million [10]. Finally, one of the most recent examples is the Canterbury earthquake sequence (2010–2011), which generated economic losses exceeding NZD 40 billion [11], while widespread liquefaction represented one of the principal causes of damage to residential land, housing, and lifeline infrastructure in Christchurch [12].

For these reasons, assessing liquefaction susceptibility is a fundamental component of land-use planning and disaster risk reduction in seismically active areas. It requires the integration of geotechnical, hydrogeological, and geomorphological data, as well as a thorough understanding of the mechanisms governing soil response to seismic loading ([13–16]).

At this regard, among the most popular qualitative methods are those proposed by Youd and Perkins [17], Wakamatsu [18], and Wakamatsu et al. [19]. In particular, Youd and Perkins collected information regarding earthquake-induced liquefaction case studies, such as the 1906 San Francisco, the 1954 Fallon-Stillwater, the 1964 Alaska, the 1964 Niigata, and the 1976 Guatemala earthquakes [20–24], and suggested the subdivision of the investigated geological units into five classes of liquefaction susceptibility referred to as ‘non’, ‘low’, ‘moderate’, ‘high’, and ‘very high’. This subdivision was based on their age, type of prevailing shallow deposits, and depth of water table. Specifically, sediments were initially grouped as continental, coastal, and artificial deposits of Modern (<500 years), Holocene (<11 ka), Pleistocene (11 ka–2 Ma), and pre-Pleistocene (>2 Ma) ages.

Following these criteria, Youd and Perkins [17] proposed that a saturated soil unit described as ‘recently deposited unconsolidated material of river channel, floodplain, deltaic, dune and estuarine formations, and uncompacted artificial fills’ should be characterized as ‘high’ to ‘very high’ susceptibility to liquefaction. On the other hand, talus, glacial till, residual soils, tuff, and compacted fills should be in general classified as ‘non-susceptible’ to liquefaction. Moreover, in this approach it is implied that liquefaction susceptibility is decreasing from Modern to pre-Pleistocene deposition.

Wakamatsu et al. [19] took into consideration the ground motion intensity and the correlation between past liquefaction sites and geomorphological conditions associated with 75 earthquakes that occurred in Japan from 1885 to 1997. In particular, they considered two levels of ground motion for the classification of geomorphological features. Level-1 ground motion corresponds to crustal earthquakes, which may occur once or twice during the lifespan of an infrastructure, while level-2 is caused by subduction events and/or generally rare great earthquakes. For example, the 1964 Niigata and 1995 Hyogo-ken Nambu earthquakes were assumed to have caused level-1 and level-2 ground motions, respectively. The suggested geomorphologically based criteria were developed with reference to the criteria for an earthquake of seismic intensity V on the Japan Meteorological Agency scale (roughly equivalent to intensity VIII on the Modified Mercalli scale). In case

of level-1 ground motion, the susceptibility to liquefaction of the geomorphological features is mainly classified as 'high', 'low', 'very low', and 'none', while for the level-2 scenario the most relevant classes are 'very high', 'high', 'low', and 'none'. In both cases, the most susceptible zones are the ones characterized by fluvial or costal sediments, such as former river channels, former ponds, point bars, artificial deposits, beaches, and lowlands between dunes. These depositional-geomorphological features are classified as 'highly' susceptible to liquefaction in the former seismic scenario and as 'very high' in the second one.

Moreover, according to several studies focused on the geomorphological characteristics of the sites where liquefaction manifestations occurred during a seismic event [25–36], it was concluded that liquefaction phenomena are not randomly distributed over an active or recent floodplain, but are strongly dependent on the depositional history of the sediments in terms of grain size distribution as well as the depositional age and the shallow layering. The above-mentioned studies document that fine- and coarse-grained sediments of Holocene age sorted by fluvial or wave actions, such as in old/abandoned channels, point bars, and coastal settings, generally exhibit a notably higher density in liquefaction occurrences than other sectors (and hence other sedimentary conditions) of the same floodplain and/or coastal area. Consequently, the reliability of a liquefaction susceptibility map is highly dependent on the scale, density, and accuracy of the geological and geomorphological mapping as well as the available hydrogeological data.

In addition, several authors have focused on the influence of site-specific hydrogeological conditions on the assessment of soil liquefaction potential [36–44]. For example, Chang et al. [38] emphasize the importance of correctly representing this parameter in analytical models, as inappropriate assumptions may significantly distort the results. In particular, assuming a 3-m higher groundwater level relative to the real one can lead to an underestimation of the Liquefaction Potential Index (*LPI*) up to 10–30%. Conversely, if the assumed level is 3 m lower than the actual depth, the *LPI* may be overestimated by 5–45%. These findings highlight the need for accurate hydrogeological characterization in seismic hazard evaluations.

Cox et al. [44] highlight the pressure changes induced by the M_w 6.2 Christchurch earthquake, observing mechanisms of groundwater transfer from deep to shallower aquifers. It is hypothesized that artesian pressures further promoted suffusion and piping along fractures, preferential flow paths, and already liquefied horizons. Following this suggestion, Dudley et al. [37] investigated the role of the confined aquifer in the mechanism of soil liquefaction due to the 7.5 M_w earthquake in Palu (Indonesia) on 28 September 2018.

Considering the above premises, this research focuses on an area characterized by the transition from fluvial–alluvial deposits of the Po Plain to deltaic sediments. These characteristics make the study area particularly suitable for investigating the lateral variability of soil liquefaction susceptibility across transitional environments between fluvial and deltaic domains.

At the local scale, our findings may serve as an operational tool to support land management and sustainable planning strategies within the deltaic area investigated, but also in similar geomorphological-geographical settings. Consistent with the United Nations Sustainable Development Goals [45], particularly SDG 11 and SDG 13, this study aims to contribute to disaster risk reduction and resilience-oriented land-use planning in vulnerable areas.

From a scientific standpoint, they offer valuable insights into the liquefaction behavior of complex deltaic environments potentially affected by seismic activity, thus contributing to the broader understanding of geohazard-related processes in such sensitive regions.

2. Study Area

The investigated region mainly corresponds to the eastern sector of the Province of Ferrara and secondarily the Province of Rovigo (northern Italy), including part of the modern Po River Delta and covers an area of about 560 km^2 (Figure 1).

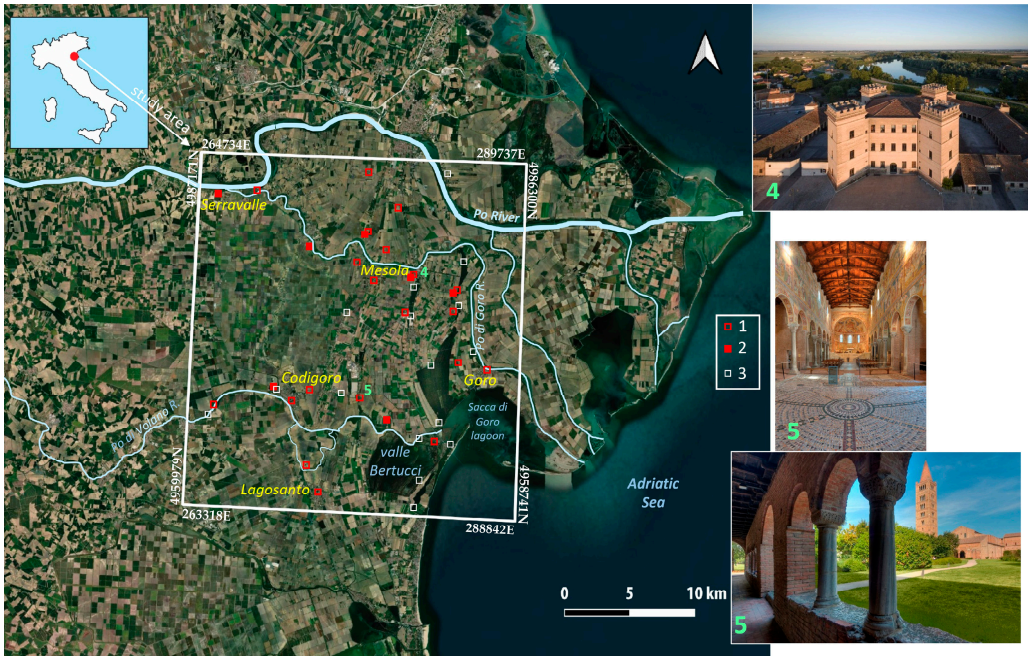


Figure 1. Study area (white square). Main architectural (**1**), archaeological (**2**), and natural (**3**) heritage sites; (**4**) Mesola Castle (1578–1583; photo from https://castellodimesola.it/; accessed on 29 April 2026); (**5**) Pomposa Abbey (Benedictine monastery, VI–VII century; photo from https://deltadelpo.eu/it/41-abbazia-di-pomposa/; accessed on 29 April 2026). The names of the main urban centers are shown in yellow. Image from Google Earth.

The Po River is the most important fluvial system in Italy, with a length of approximately 650 km, draining a catchment area of about 75,000 km^2. It flows into the northern Adriatic Sea, contributing to the development and maintenance of the modern Po Delta (Figure 1).

The territory is characterized by the dominance of intensive agricultural activities and hosts important cultural, archaeological, and natural heritage assets (e.g., the Mesola Forest—called *Bosco della Mesola*, the Mesola Castle and the Pomposa Abbey; Figure 1). Moreover, a significant portion of the territory lies below sea level (ranging from −3 to 0 m, *slm*). Consequently, a dense network of reclamation canals connected to several pumping stations (known as *idrovore*) has been developed to facilitate water discharge towards the Adriatic Sea. These canals perform a dual function: they serve as irrigation infrastructure during the summer months and as a drainage system for rainwater during the winter season. The presence of water has favored agricultural development; monoculture dominates (maize, sugar beet, corn, soybean, poplar), followed by horticultural and viticultural cultivation, while rice farming is practiced in some sectors.

The territory is affected by rapid subsidence and high sediment input, which have allowed for the preservation of a well-stratified record of the late Quaternary transgressive–regressive sedimentation cycles. In coastal sectors, Holocene sediment thickness can exceed 40 m. As a result, the area is characterized by complex alluvial systems, coastal dune ridges, and sandy bars, which are sometimes connected to littoral spits enclosing extensive lagoonal environments.

2.1. Geological, Geomorfological, and Hydrogeological Setting

The geological, geomorphological, and hydrogeological setting of the study area reflects the combined influence of multiple natural and anthropogenic factors. This complex system has evolved through the interplay of:

(a) tectonic activity, characterized by active ramp-and-flat reverse faults structurally characterizing the subsoil of the broader Po Basin and Adriatic Sea;
(b) alternating climate conditions during the Quaternary has strongly influenced erosion processes in the surrounding Alpine and Apennines mountain chain, therefore determining the amount and nature of the sedimentary successions within the foredeep and foreland areas, including the investigated one [46–48];
(c) fluvial and deltaic processes, including recent hydrographic evolution such as channel migration and variations in sediment supply, closely linked to the late Holocene dynamics of the Po River system;
(d) anthropogenic modifications, encompassing extensive land reclamation, construction of river embankments, and channelization, predominantly initiated during the Early Modern period;
(e) subsidence phenomena, both natural (tectonic and compaction-related) and anthropogenic in origin, which have significantly contributed to the lowering of the topographic surface across various sectors of the delta plain. Between the 1950s and the early 1970s, the extraction of large quantities of methane-rich groundwater caused up to 3 m of land subsidence, with maximum land subsidence rates reaching 300 mm/a during the period 1950–1957 [49] in the innermost part of the delta, where the main pumping centers were located.

2.1.1. Geomorphological Evolution

The palaeogeographic and hydrographic evolution of the Po Plain has been deeply conditioned by long-term climatic oscillations (6000 yr BP; Figure 2) that affected the entire Mediterranean basin. In periods of increased precipitation, such as during humid climatic phases, the lower Po Plain was crossed by a dense and active fluvial network. These hydrological conditions favored the widespread deposition of alluvial sediments and the formation of coastal dune systems due to enhanced sediment supply and channels mobility. Conversely, during warm and arid climatic intervals, river discharge was significantly reduced. Simultaneously, global sea-level rise—driven by glacial melting—caused the shoreline to retreat inland, strongly altering the coastal configuration.

At the base of these fluvio–deltaic transformations lies a fundamental sedimentological and diagenetic process. Rivers tend to deposit coarse-grained sediments, such as sands and gravels, along their main channels, while finer materials (silts and clays) are distributed laterally, thus contributing to the formation and growth of natural levees. During flood events, overbank flows deposit coarser sediments near the active riverbeds, while the finer-grained fractions, suspended in floodwaters, are transported into more distal and more depressed areas. The latter zones, often corresponding to wetlands or marshes, are characterized by anoxic or poorly oxygenated conditions that favor the accumulation of organic matter and with time the formation of peat-rich deposits.

The reconstruction of the hydrographic evolution of the lower Po River over the last 3000 years has been made possible on the basis of an interdisciplinary approach, integrating historical research, archaeological findings, and geomorphological analyses [50–54]. In addition, the study of historical cartography has played a fundamental role in identifying past river courses, palaeochannels, and avulsion processes.

Figure 2 illustrates one of the key phases of this hydrographic evolution, highlighting the interactions between fluvial dynamics and climatic forcing from the maximum transgression period (about 5500 BP) to about 200 BP.

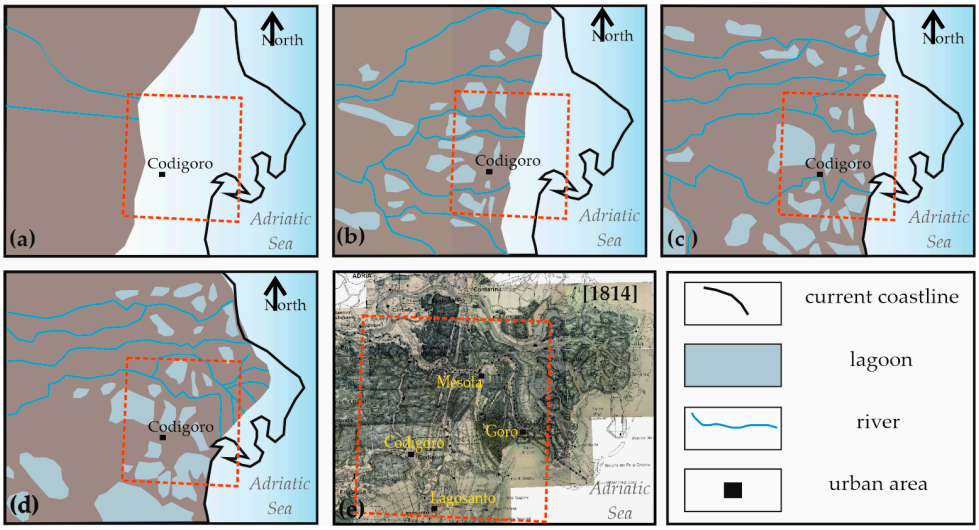


Figure 2. Hydrographical and geomorphological evolution of the Po River Delta (modified from Veggiani, [55]): (**a**) about 5500 BP, it is evident that a substantial part of the study area was previously occupied by marine environments; (**b**) 2300 PB; (**c**) 600 BP; (**d**) 200 BP; (**e**) historical map (1814; il territorio ferrarese). The solid black line represents the current coastline, whereas the brown-shaded areas correspond to the mainland. The study area is indicated by the red dashed box.

2.1.2. Surface Geology

From a depositional environment standpoint (Figure 3), the study area occupies a transitional zone between delta plain deposits (fluvial and fluviolacustrine formations) and those of the delta front and associated sandy flats (coastal and lagoonal formations).

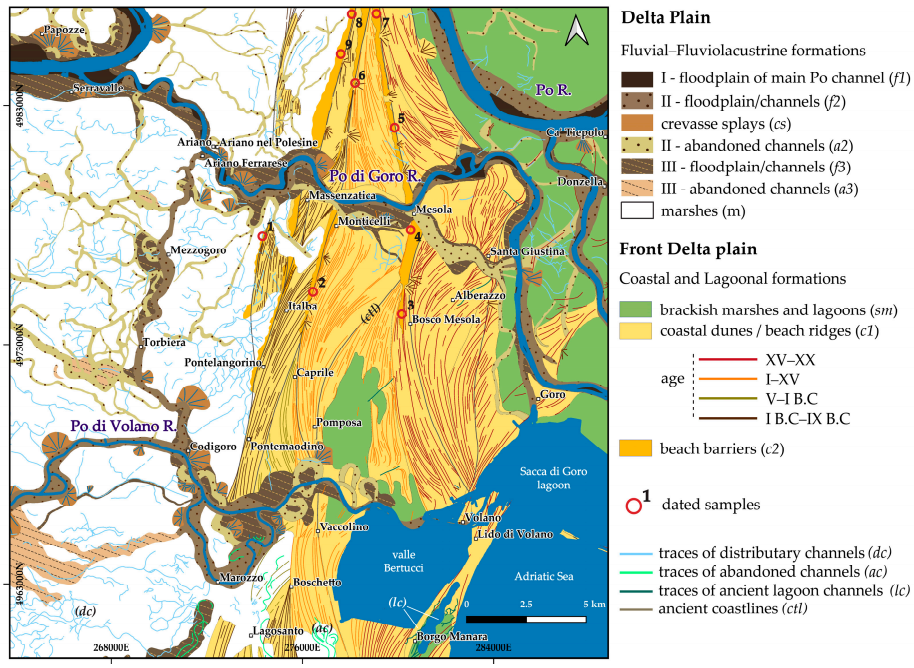


Figure 3. Geological map of surficial sediments (re-elaboration based on Servizio Geologico d'Italia, [56]). See text for detailed descriptions of mapped units. The age of the dated samples is reported in Table S1. The names of the main urban centers are shown in black.

Fluvial and Fluviolacustrine Formations—Ravenna Subsystem (AES8)

The AES8 unit is composed of clays, silts, and sands of deltaic and marine origin. Its thickness ranges from approximately 20 m in the western sector to about 40 m in the eastern sector. These deposits are Holocene and were accumulated from around 10,000 years B.P. to the present. In the western sector, marsh deposits (*m* unit) prevail covering depressed inter-distributive areas between mainly suspended river channels with their natural levees (*f1* and *f2* units) and crevasse splay (*cs* unit) bodies. These marshy areas, generally with an altitude of some meters below sea level, have been drained by extensive hydraulic reclamation activities carried out in several steps during the last centuries. In these reclaimed lands mainly clays and silty clays presently crop out with alternating thin silty levels; they are often rich in organic material, locally fading into peaty clays and peats. Scattered bioclasts of continental Molluscs and abundant woody fragments are also present. Internal depositional features and layering are frequently obliterated by intense bioturbation, while a dense plane-parallel lamination or thin sandy-silt layers graded by distal fluvial overflow processes could be locally preserved. Further sedimentary aggradation was completely halted by hydraulic reclamation works. At present, these deposits cover a cumulative surface of ca. 225 km^2, representing the 33% of the investigated area. Thickness of the formation locally reaches 15 m.

Coastal and Lagoonal Formations—Modena Unit (AES8a)

The Modena Unit (AES8a) represents the uppermost and most recent portion of the AES8 succession, consisting of deltaic clays, silts, and sands. Its basal boundary is defined to the east by an ancient, distinct, and predominantly erosional shoreline, and to the west by the transition between alluvial plain and deltaic deposits.

The unit is defined as post-Roman and has been identified based on the hydrographic reorganization, the enhanced sedimentation rates, and changes in archaeological signatures associated with the collapse of the Roman Empire. In its eastern sector, it includes delta-front and beach deposits, some of which are still undergoing active depositional processes. The thickness of this unit varies between 0 and 25 m, and its age ranges from approximately 1500 years B.P. to the Present.

Towards the east, the fine-grained deposits, associated with dominant marshy conditions environments, are progressively overlain by coastal dune and beach ridge deposits (*c1* unit). The latter deposits consist of medium- to fine-grain sands, rich in bioclasts and wave structures, organized in thin- to medium-thickness layers frequently amalgamated. Faunas include Molluscs and Foraminifera commonly concentrated in storm deposits. Based on the observed sedimentary features and the faunal associations, it is possible to recognize lateral and vertical *facies* changes and hence distinguish between offshore and more internal settings.

External delta sediments consist of land of coastal dunes and beach ridges (*c1* unit), beach barriers (*c2* unit) and interposed brackish marshes, and lagoon depositional environments (*sm* unit). The central–eastern sector of the investigated area is characterized by coastal plain sands. They record several delta lobe generations, with outcropping littoral sediments that often preserve their primary morphology. These sands are locally interfingering with the deposits associated with the terminal section of several distributary channels intersecting the area.

These coastal deposits are locally associated with elongated beach barriers (*c2* unit) running parallel to the beach ridges. These beach barriers consist of very well sorted fine sands lacking bioclasts (except from sporadic pulmonated Gastropods). Coastal dune and beach ridges cover a surface of 171.6 km^2 corresponding to the 27.6% of the investigated

area, while the outcropping beach barriers only 10 km^2 (1.6%). For the purpose of this note, these sedimentological details will not be discussed further.

Moreover, the eastern and northeastern sectors are covered by the brackish marshes and lagoons deposits (*sm* unit) associated with the current Po River delta, while smaller courses of limited width were classified as traces of ancient lagoon channels. These units (67.4 km^2) consist of clays, silty clays, and clayey silts, often enriched in organic substances and with subordinate intercalations of sandy-silty layers graded by distributary channel routes. Most of these environments are still subject to active sedimentary dynamics. These fine sediments form bodies on coastal sands up to a few meters thick in the southeastern part of the area, while in the northeastern sector similar sediments form much thicker and more extensive bodies with a base on pro-delta muds.

2.1.3. Hydrogeology of the Area

From a hydrogeological point of view, the following aquifer systems can be identified (Rapti-Caputo and Martinelli, 2009 [57]; Marrocchino et al., 2010 [58]; Rapti and Martinelli, 2025 [59]):

(a) In the central–eastern sector, a shallow phreatic (unconfined) aquifer system is hosted within sandy coastal–deltaic bodies of the delta-front plain, including dune ridges, beach ridges, and beach–barrier complexes (Figure 3). This aquifer exhibits pronounced lateral and vertical heterogeneities due to facies variability typical of these depositional environments. It is characterized by relatively high hydraulic conductivity and a thickness ranging from a few meters up to approximately 20 m, depending on local stratigraphic conditions. Recharge is primarily controlled by direct meteoric infiltration, while secondary contributions derive from hydraulic interaction with irrigation canals and adjacent surface water courses. Water depth data indicate that the water table undergoes seasonal to interannual fluctuations generally ranging from 75 to 125 cm (88% of the data) below ground level with rare exceptions where the level reaches 300 cm (Figure 4a). Specifically, 10% of the data show a water depth exceeding 125 cm, whereas in 2% of the cases it is below 75 cm.

(b) Within the alluvial plain and lagoon deposits, dominating the western sector but also present in the eastern part of the study area (Figure 3), small unconfined or semi-confined aquifers develop, which may be hydraulically interconnected. These aquifers consist of sandy or sandy-silty materials with local intercalations of peaty layers. Their thickness is a few meters and they have low productivity. In general, the water depth exhibits both annual and multi-year fluctuations, ranging from 15 to 300 cm from the ground surface (Figure 4b). In particular, 31% of the analyzed sites exhibit a water depth ranging from 0.5 to 150 cm, whereas 65% fall within the 150–300 cm range.

The observed piezometric conditions reflect the integrated response of several local controlling factors, including: (a) the hydrostratigraphic architecture and hydraulic properties of the aquifer systems; (b) groundwater recharge conditions—particularly in areas close to the dense irrigation channel network, where groundwater depth is strongly controlled by channel water levels; and (c) groundwater abstraction rate, which may locally and temporarily alter piezometric level conditions. Accordingly, the distributions presented in Figure 4 should be interpreted as a regional representation of the hydrodynamic behavior of the study area and not as a probabilistic characterization directly attributable to the individual depositional units adopted in the Liquefaction Potential Index assessment. The influence of water depth fluctuations on liquefaction susceptibility will be examined in Section 4.

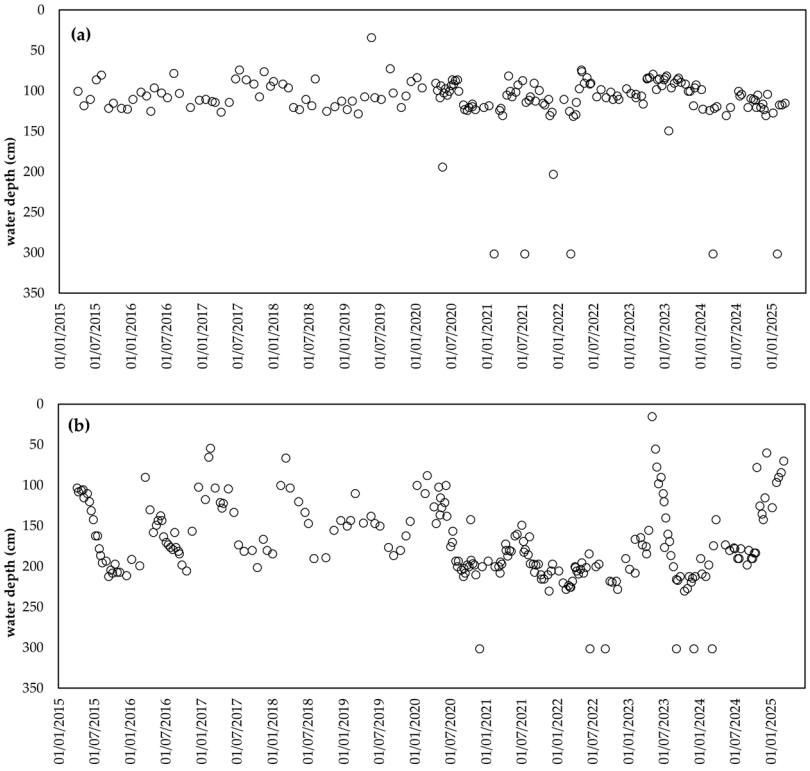


Figure 4. Examples of time variation of the ground water depth (expressed in cm below ground level) in the observation monitoring point. For (**a**,**b**), see the explanation in the text.

3. Materials and Methods

To achieve the objective of this research, the methodological flowchart illustrated in Figure 5 was adopted. It is structured into three main phases. The first phase involves the collection and critical analysis of geological, geomorphological, hydrogeological data, as well as historical cartography. The definition of the geomorphological features of the depositional systems and the associated surface lithology was mainly based on the Geological Map of Italy at a 1:50,000 scale, Codigoro sheet no. 187 [56], integrated with other sedimentological data (e.g., [60]), data from geognostic investigations (11 boreholes and 144 penetrometer tests; Figure 6), and laboratory analyses (grain-size analyses).

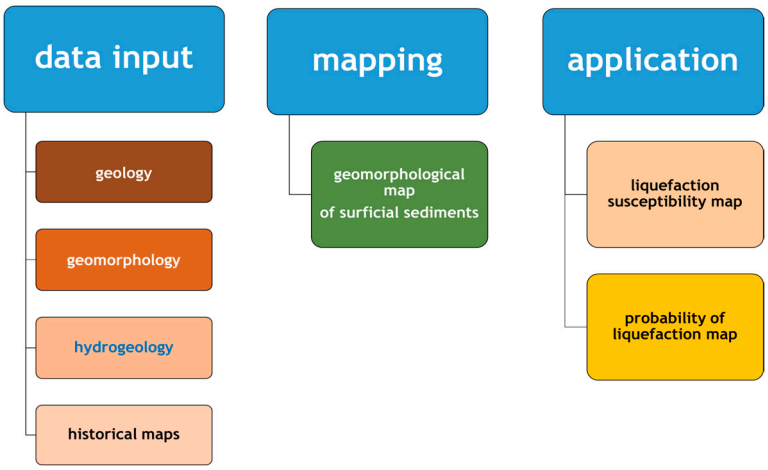


Figure 5. Flowchart showing the principal working phases of the method applied in this study for the compilation of geological map of surficial sediments, assessment of liquefaction susceptibility, and the probability of liquefaction. The results are presented in Section 4 and discussed in Section 5.

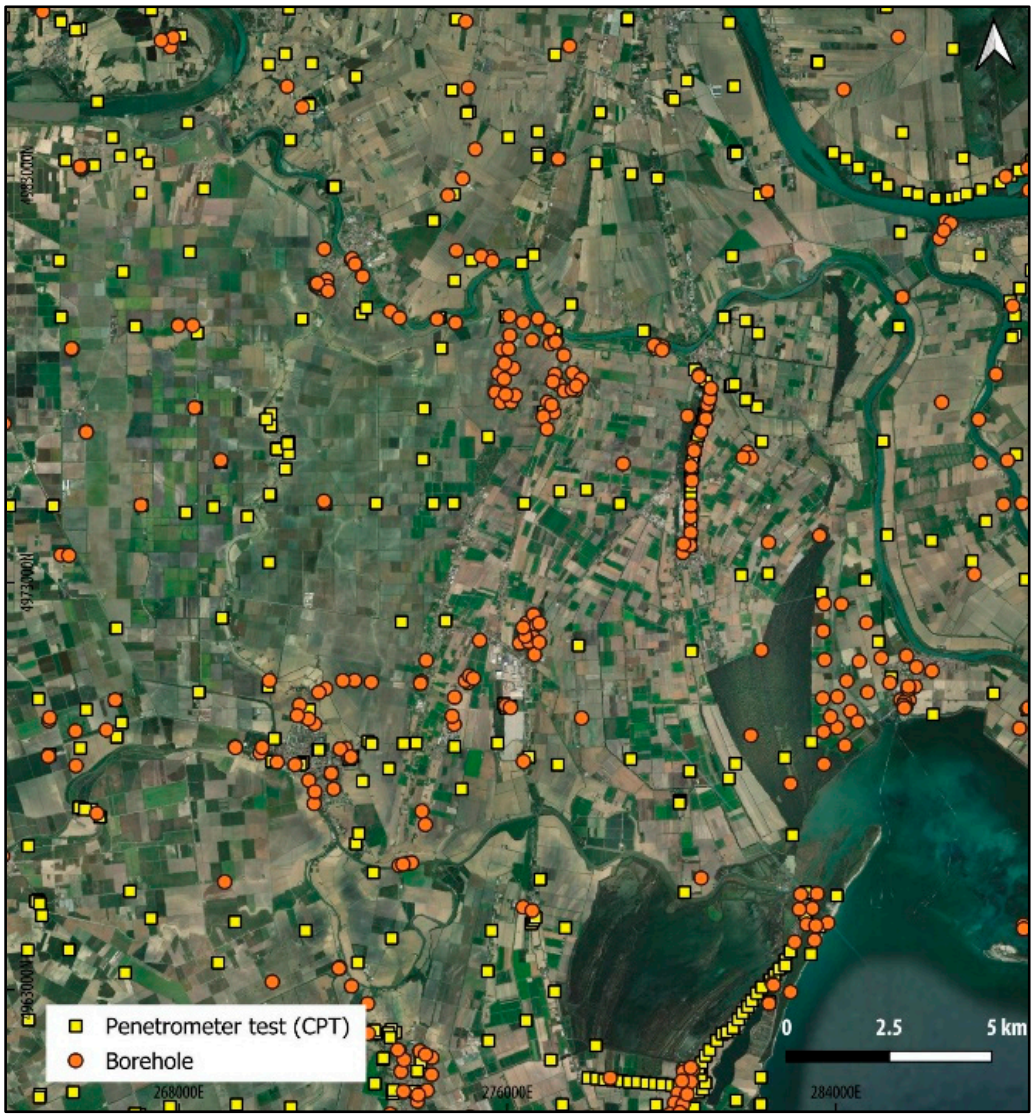


Figure 6. Spatial distribution of penetrometric and borehole data (source: Emilia-Romagna database).

The second phase concerns the elaboration and spatial distribution of the main parameters of interest. The third phase consists in the development of soil liquefaction susceptibility and probability maps, based on the integration of the previously analyzed data.

In this section, we present the principal methods applied in this paper to achieve the intermediate steps and then the final results for reaching the major goals of the research. In particular, we will (i) describe how to obtain a susceptibility map from the geological map of the shallow lithologies and the shallow hydrogeological conditions; (ii) how to estimate the maximum expected peak ground acceleration that could affect these sedimentary units assuming a worst-case (i.e., conservative) seismic scenario; and from these, (iii) how to estimate the probability of liquefaction across the entire investigated area. Finally, considering Cone Penetration Tests with pore pressure measurements (CPTu), we will investigate the correlation between the obtained liquefaction susceptibility classification of sediments with the values of liquefaction potential derived from in situ tests. Following the description of the methodological approaches at each step is also presented.

3.1. From Lithology to Susceptibility

The classification proposed by Youd and Perkins [17] has been applied to a sector of the Po delta plain, for examining the likelihood of geological units to liquefaction. According

to the criteria proposed by the authors, the deposited materials of the floodplain/channels (*f1*, *f2*, *f3*) and crevasse splays (*cs*) have been grouped as 'floodplain deposits'. Abandoned channels (*a2*, *a3*) and their associated traces have been also classified as 'river channels'. Moreover, marsh deposits (*m*) founded in inter-distributive areas were classified as alluvial plain, while front delta deposits of brackish marshes, lagoons (*sm*), and traces of lagoon channels were categorized as lagoonal deposits. Finally, formations of coastal dunes/beach ridges (*c1*) and beach barriers (*c2*) have been included in dune and estuarine deposits, respectively.

As it concerns the age of the sediments, Youd and Perkins [17] classify the units in the categories of (a) <500 years, (b) Holocene, (c) Pleistocene, and (d) pre-Pleistocene. In our case, the whole study region is covered by Holocene deposits, with the most recent ones recognized in the evolving floodplain of the principal branch of the Po channel (*f1*) and in the front delta plain area. Accordingly, formations of class I-floodplain (*f1*), brackish marshes, and lagoon as well as coastal dunes of the XV–XX centuries are certainly younger than 500 years. In agreement with the statement that younger sediments are looser and consequently more likely to experience liquefaction in saturated conditions [61], and considering the Youd and Perkins [17] criteria, the floodplain of the principal channel of the Po River (*f1*) could be classified as a uniform zone of high susceptibility, based on the geomorphological map used for the preliminary purposes of this research. Table 1 presents a summary of the classification of the different units recognized in the investigated area (Figure 3) according to Youd and Perkins [17].

Table 1. Classification of liquefaction susceptibility of surficial geological units included in the map of Figure 3 based on the criteria proposed by Youd and Perkins ([17]; grey-highlighted) and a refined classification proposed in the present paper. Areas are in km^2. Susceptibility classification: VH = very high; H = high; M = moderate; L = low; Non = non-susceptible.

Geological Units	Area	Youd and Perkins [17]			Present Work
I—floodplain of main Po channel (*f1*)	21.2	<500 yr	floodplain	H	VH
II—floodplain/channels (*f2*)	40.4	Holocene	floodplain	H	H
crevasse splays (*cs*)	12.0	Holocene	floodplain	H	H
II—abandoned channels (*a2*)	35.9	Holocene	river channel	H	H
III—floodplain/channels (*f3*)	28.8	Holocene	floodplain	M	M
III—abandoned channels (*a3*)	9.8	Holocene	river channel	M	M
marshes (*m*)	225.1	Holocene	alluvial plain	L	Non
brackish marshes and lagoons (*sm*)	67.4	<500 yr	lagoonal	L	Non
coastal dunes/beach ridges (*c1*)	171.6	<500 yr	dune	H	H
		Holocene	dune	M	M
beach barriers (*c2*)	10.0	Holocene	estuarine	M	M

It is worth to note that several studies of the last 20 years suggest that in contrast to an apparently uniform fluvial floodplain liquefaction occurrences are strongly correlated, and show important variations, in correspondence with, for example, abandoned channels and point bars [27,31,33,34,62]. At this regard, Wakamatsu et al. [19] also proposed that the deposits be located in the inner part of a meander, i.e., point bars deposits, which should be classified as separate units associated to a very high liquefaction susceptibility category in case of level 2 ground motion. In line with these suggestions and following the initial classification of surficial units, it was assumed that these parts of the floodplain of the main Po channel (*f1*) should be upgraded from high to very high susceptibility to liquefaction (Table 1).

As it concerns the assessment of liquefaction susceptibility for the 'floodplain/channels' formations (*f2* and *f3*), their classification was based on both the relative age and the depositional material. Even though the *f2* unit consists of sandy material similar to *f1* and likely younger than 500 years, it has been differently characterized as highly susceptible due to the older age and the inactive depositional environment. Following the same principle, *f3* deposits have been classified as moderate susceptibility, due to the fact that they are mainly composed of silty-sandy material of Holocene age. Furthermore, formations of abandoned channels *a2* and *a3*, as well as crevasse splay deposits were classified in accordance with their associated floodplains as high and moderate susceptibility, respectively.

On the other hand, estimation of the absolute chronology of coastal dunes and beach ridges *c1* resulted in a further distinction of their susceptibility to high and moderate class, with units of the XV–XX centuries included in the former class. Moreover, beach barrier formations were characterized as Holocene estuarine deposits, therefore they were associated with a moderate liquefaction susceptibility class. Finally, marshes of interdistributary areas and brackish marshes and lagoons of front delta plain were classified as non-susceptible features, since they basically consist of clays, silty clays, and silts.

3.2. Seismic Input

The investigated area is adjacent to the seismogenic zone 912 of the SZ9 seismic zonation map of Italy [63], which generated several seismic events in historical times, including the 1570 Ferrara, 1574 and 1639 Finale Emilia, 1901 Mirandola [64–66] as well as the 2012 Emilia earthquakes (e.g., [67]). This zone has been geometrically defined and seismologically and seismotectonically characterized on the basis of the regional tectonic and geological setting of the broader Po Plain. In zone 912 several blind reverse faults have been identified capable of generating moderate earthquakes (Meletti et al. 2004 and references therein [63]). For the purpose of a probabilistic seismic hazard assessment analysis, in the national map it is also indicated for each zone the maximum expected magnitude, M_w, the corresponding rupture mechanism (faulting type), and the most likely range for the hypocentral depth. In zone 912, an M_w = 6.14, a reverse kinematics, and an interval depth of 5–8 km are suggested.

It should be noted that our investigated area falls outside any seismogenic zone of the national map and hence the maximum expected PGA values at the different locations must be calculated to obtain a reference triggering seismic load for the evaluation of the liquefaction potential at any point. Following the 2012 seismic sequence with an M_w = 6.1 mainshock and several events greater than 5 [67], the recorded ground motions have been nicely reproduced by the ITA10 attenuation law [68], which could be accordingly considered suitable for the Po Plain geological setting [69]. Due to the similar geological conditions, ITA10 [68] could be therefore applied also to the area investigated in the present paper. This attenuation law combines a nonlinear term for the distance from the epicenter (F_D), a linear term for the scaling of the magnitude (F_M), a site coefficient for including lithological amplifications (F_{soil}), and a coefficient related to the faulting style (F_F).

$$\log_{10} \mathrm{PGA} = e_1 + F_D(R, M) + F_M(M) + F_{soil} + F_F \quad (1)$$

where the distance function is defined as

$$F_D(R, M) = \left[c_1 + c_2\left(M - M_{ref}\right)\right] \log_{10}\left(\frac{\sqrt{R_{JB}^2 - h^2}}{R_{ref}}\right) - c_3\left(\sqrt{R_{JB}^2 - h^2} - R_{ref}\right) \quad (2)$$

where R_{JB} is the Joyner–Boore distance and h the depth, while the magnitude function is

$$F_M(M) = b_1(M - M_h) + b_2(M - M_h)^2 \quad (3)$$

Bindi et al. [68] fix the parameters R_{ref} = 1 km, M_{ref} = 5.0 and M_h = 6.75. In order to apply Equation (1) to the whole investigated area we have subdivided it into a regular grid. Taking into account the details and the minimum dimensions of the mapped lithological units due to the scale of the basic input data (Figure 3), a good compromise between running time and resolution of the output products is achieved with a mesh size of 50 m × 50 m. Accordingly, beyond the constant coefficient e_1, posed equal to 3.672, and assuming the same reverse faulting style for the entire investigated area (F_F = 0.105), the expected PGA was thus calculated for each mesh by assuming the centroid of the cell as a possible epicenter. At this regard, it should be noted that our investigated area falls outside any seismogenic zone of the national SZ9 zonation map, while the closest zone is the 912 almost contiguous to the SW corner.

In order to assume a reasonable magnitude value for each cell of the grid, we explored a broad set of seismic scenarios, for a first set of models a negative gradient has been applied, tentatively following a linear decrease of 0.03 M_w units per kilometre of distance from the border of the 912 zone [63], (Figure 7a). Although we tested different magnitude gradients (see Figure S1 in Supplementary Materials), the above gradient assures that the minimum magnitudes in the NE corner of the investigated area roughly corresponds to 5.0, which represents the background seismicity commonly assumed in SHA analyses in Italy.

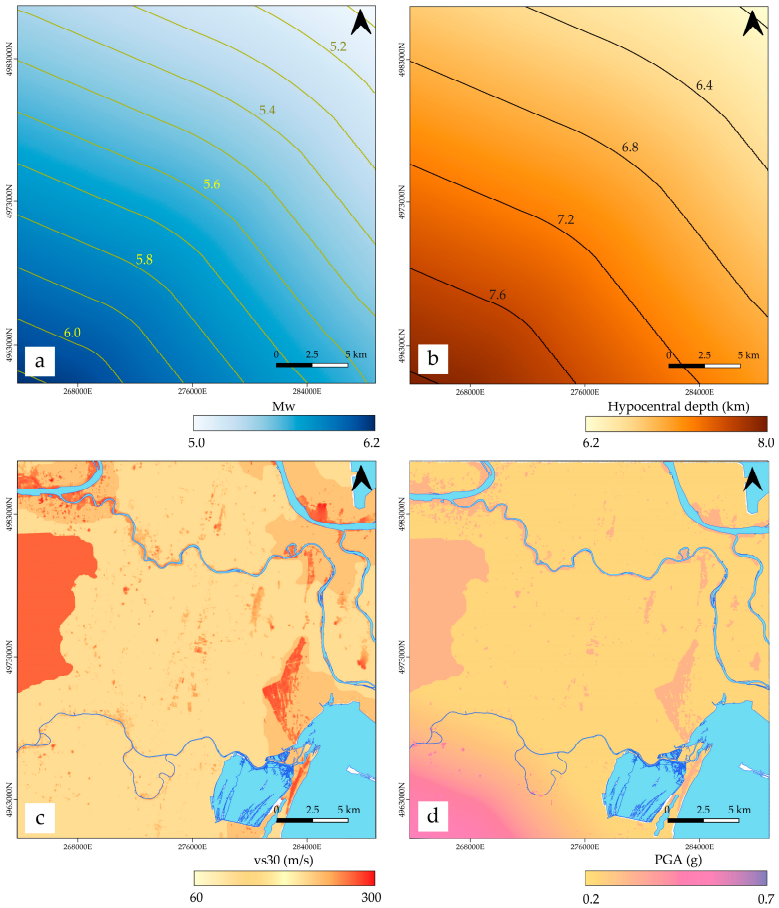


Figure 7. Examples of magnitude (**a**) and hypocentral depth (**b**) distribution for one of the selected double gradient models (see text). (**c**) Distribution of the v_{s30} [70]. All values within the investigated area range between 150 and ca. 250 m/s. (**d**) Calculated PGA values (in fraction of g) based on the preferred seismic input model and applying Equations (1) to (4).

As concerns the lithological amplification coefficient, F_{soil}, in Equation (1) we analysed the available v_{s30} map produced by Mori et al., [70], showing that the investigated area is entirely characterized by values between 150 and ca. 250 m/s corresponding to soil class *C* (>180 m/s) and *D* (<180 m/s) (Figure 7c). With the same systematic procedure, for this parameter we thus attributed to the coefficient F_{soil} of each cell the corresponding value of 0.240 and 0.105 for soil class *C* and *D*, respectively (Figure 7c; [68]).

Having assumed as a worst-case scenario that each cell corresponds to an epicenter, the Joyner–Boore distance is accordingly posed equal to 0, and the distance function F_D simplifies as follows:

$$F_D(R, M) = [c_1 + c_2(M - 5.5)]\log_{10}(h) - c_3(h - 1) \quad (4)$$

Relative to the depth, we considered two possible hypocentral conditions. Firstly, we assumed a value of h = 10.322 km as proposed by Bindi et al. [68] from the regression of the entire dataset, which would further simplify Equation (4). Alternatively, based on the tectonic setting in correspondence of the investigated area, which is on top of the frontal most sector of the Northern Apennines orogenic wedge (e.g., [46]), the shallower possibly seismogenic source could be represented by the low-angle basal detachment and associated splay faults. Corresponding depths for these structures progressively decrease NNE-wards from 8 to 6 km [46,71]. Further seismogenic sources could be represented by inherited high-angle structures affecting the underlying units formally belonging to the Adria plate thus potentially generating hypocentral depths comparable to the above-mentioned fixed h value (10.322 km). Following the worst-case scenario approach of this research, we accordingly tested the depth variable condition in the calculations of the PGA (Figure 7b).

As an alternative to the double gradient models (NNE-wards decrease of the magnitude and shallowing of the hypocentral depth) above described, we recall that for the areas outside the Italian seismogenic zones SZ9, a reference background seismicity with magnitude 5.0 is assumed [72]. Accordingly, in a second group of models the PGA was calculated for each mesh by assuming the centroid of the cell as a possible M5.0 epicenter. Furthermore, in this case we tested different fixed focal depths between 6 and 8 km (see Figure S2 in Supplementary Materials). Similar to Norini et al. [69] we also tested the scenario of an event of fixed magnitude (M = 6.14) occurring at the closest point of the 912 seismogenic zone, where the PGA values at each mesh of the grid 'simply' decrease with distance according to Equations (1) to (4) (Figure S2d in Supplementary Materials).

Following several tests to evaluate the sensitivity of the models to the selected parameters, we finally considered a composite model characterized for each mesh by the greatest calculated PGA value between assuming an M = 6.14 event occurring within the 912 seismogenic zone at the SW corner of the investigated area and a 'local' 5.0 magnitude associated to the background seismicity outside the zone 912. This represents our preferred model for the seismic input. Accordingly, based on the above assumptions and equations, the maximum expected PGA has been therefore calculated for each cell of the grid (Figure 7d).

3.3. Liquefaction Probability Estimates

In order to estimate the probability of liquefaction, the method proposed by HAZUS [73] was subsequently applied. According to HAZUS, the likelihood of experiencing liquefaction at a specific location is primarily influenced by (a) the susceptibility of the soil, (b) the amplitude and duration of the ground shaking, and (c) the depth of the groundwater. Therefore, geological units susceptible to liquefaction and a seismic scenario were considered in assessing the probability of these phenomena.

Specifically, taking into consideration the susceptibility categories of Table 1, a mean groundwater depth of 0.5 m (Figure 4) as the most conservative scenario, a moment magnitude ranging from 5.0 and 6.14 (Figure 7a) and maximum expected PGA between 0.31 and 0.67 g (Figure 7d), the probability of liquefaction was determined by the following equation:

$$P[Liquefaction_{sc}] = \frac{P[Liquefaction_{sc}|PGA = a]}{K_M \cdot K_W} \cdot P_{ml} \quad (5)$$

where P [$Liquefaction_{sc}$ | PGA = a] is the conditional probability of liquefaction occurrence for a given susceptibility category (sc) depending on the specified level (a) of peak ground acceleration (PGA).

Relationships between liquefaction probability and PGA for the different susceptibility categories are based on widely accepted empirical methods and statistical modeling of the liquefaction database developed by Liao et al. [74]. P_{ml} represents the proportion in the map of the selected unit susceptible to liquefaction, corresponding to 0.25, 0.20, 0.10, and 0.005 for the very high, high, moderate, and low susceptibility classes, respectively. As concerns the denominator of Equation (5)

$$K_M = 0.0027 \cdot \mathrm{M}^3 - 0.0267 \cdot \mathrm{M}^2 - 0.2055 \cdot \mathrm{M} + 2.9188 \quad (6)$$

corresponds to the correction factor for the moment magnitude (M), while

$$K_W = 0.022 \cdot d_W + 0.93 \quad (7)$$

represents the correction factor for the groundwater depth (d_W). The results obtained with less conservative groundwater depth values (1.5 and 3.0 m) are described and discussed in the Supplementary Materials (see Figure S3).

3.4. Liquefaction Potential

The evaluation of liquefaction potential was accomplished by collecting and analyzing data provided by in situ tests like Cone Penetration Tests, with pore pressure measurements (CPTu) conducted within the studied area. The aim of this activity was to develop a dataset of in situ tests representative for each liquefaction susceptibility class and to evaluate the liquefaction potential at different sites. Specifically, a total number of 73 CPTu were collected of which 31 were conducted on areas classified with high susceptibility, 23 moderate, and finally 19 non-susceptible to liquefaction areas.

The liquefaction potential for each analyzed CPTu, in terms of Liquefaction Potential Index (*LPI*), was computed using the CLiq3.0 software developed by Geologismiki (www.geologismiki.gr, accessed on 29 April 2026) considering the equation suggested by Iwasaki et al. [75,76]:

$$LPI = \int_0^{20} F \times w(z) dz \quad (8)$$

where F is equal to $1 - FS$, for $FS < 1$, and to 0, for $FS \geq 1.0$, with FS representing the factor of safety. The parameter $w(z)$ is equal to 10–0.5·z, with z corresponding to the depth below the ground surface (in meters). The *LPI* ranges from 0 to 100.

Initially, the factor of safety for each soil layer was estimated using the Boulanger and Idriss [77] simplified procedure, where the soil Fines Content (*FC*) was obtained based on the proposed correlation between *FC* and the soil behavior type index *Ic*. According to the recommendation of Robertson and Wride [78], soil layers with *Ic* values greater than 2.6 should be assessed as clay-like soils and consequently as non-liquefiable ones. In terms of seismic loading, we considered the earthquake magnitude and PGA values for each investigated pixel as they have been described in a preceding section. Considering the

seasonal fluctuation of the groundwater table, we tested three different scenarios: 0.5 m, as the more conservative one, related to heavy rain period and/or flooding periods, but also 1.5 and 3.0 m representing dryer seasons.

The computed *LPI* values were further statistically analyzed in terms of average values and by applying the approach of box–whisker plot method using the SPSS software (IBM SPSS Statistics 29.0.2) (see Section 5). The latter method is commonly applied for displaying the spread of the data distribution, where the rectangle indicates the first, Q1, and third, Q3, quartiles, the whiskers outside the box show the minimum and the maximum values, and the line within the box represents the median. Values that lie more than one and a half times the length IQR (= Q3 − Q1) are called outliers and are indicated as an open circle.

4. Results

4.1. Liquefaction Susceptibility Map

Based on the criteria and the methods described in the previous section, a map of liquefaction susceptibility has been produced by gridding the investigated area (Figure 8). Accordingly, each mesh of the grid was categorized into the three susceptibility classes (very high, high, and moderate susceptible units), while sectors where liquefaction phenomena are not expected or are not of interest ('Non susceptible') were also distinguished.

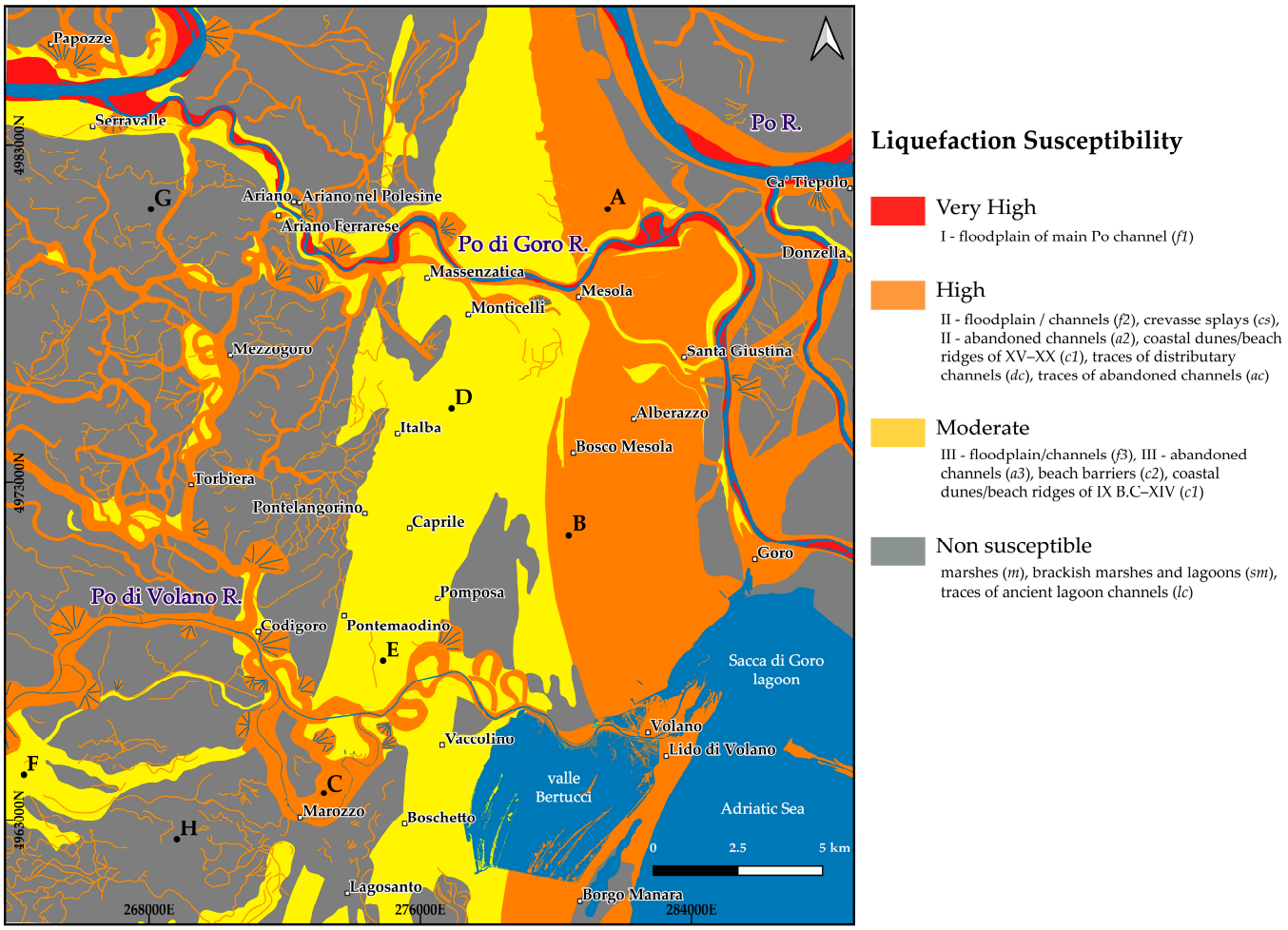


Figure 8. Liquefaction susceptibility map based on the proposed refined classification of Youd and Perkins [17] criteria (Table 1). A, B, . . ., H: indicate the location of the selected CPTu represented in Figure 12.

Following the obtained results, the most susceptible sectors (very high susceptibility class) correspond to the narrow floodplain *f1* associated to the main channel of the Po River extending from the northwestern to the central–eastern part of the investigation area (Figure 3). This unit crosses the western marsh deposits *m* and the longitudinal central sector of coastal formations and the easternmost brackish marshes and lagoons *sm*.

The western sector of the investigated region is dominated by clayish and silty clayish materials of the reclaimed marshy lands corresponding to non-susceptible units and representing a sort of background irregularly crossed by braided and/or meandering bodies defining high and moderate susceptibility narrow zones. In particular, floodplain/channels *f2*, abandoned channels *a2*, crevasse splay *cs* and narrower distributary channels correspond to highly susceptible zones, while floodplain/channels *f3* and their associated abandoned channels *a3* to a moderate susceptibility class, largely represented in the southwestern part of the map.

Towards the central-eastern sector of the area, marshy conditions are largely overlaid by coastal formations, while fluvial deposits *f1* of a major reach of the Po and floodplain/channels *f2* interlay and cross the northern and southern sectors. Being mostly covered by units formed as coastal dunes/beach ridges *c1* and beach barriers *c2*, this broad longitudinal sector was classified into two roughly parallel moderate and high susceptible zones also taking into account the different age between the inner-older and the outer-younger (<500 years) coastal dunes/beach ridges *c1*.

Coastal formations also include areas of brackish marshes and lagoons *m* located in the (north) easternmost sector of the map. Accordingly, these areas were characterized as non-susceptible to liquefaction phenomena as they are covered by deposits similar with the marshes of the western part, just differing for the higher salt content. In addition, this zone is also crossed by the major channel of the Po River (*f1*), which is associated with floodplain/channels (*f2*, *f3*) and abandoned channels (*a2*, *a3*) crossing the area similar to the western and central sectors. As a consequence, these belts were also classified as susceptible to liquefaction (very high and high).

4.2. Liquefaction Probability Map

Liquefaction susceptibility refers to the intrinsic predisposition of a soil deposit to liquefy during an earthquake whereas liquefaction probability quantifies the likelihood that liquefaction will occur under specified seismic loading conditions [16,79].

As above mentioned, in order to estimate the liquefaction probability, we applied the methodology proposed by HAZUS [73] considering the PGA values calculated in the previous section on the basis of the attenuation law recommended by Bindi et al. [68]. Within the investigated area, on the basis of the preferred seismic input model and a worst-case scenario, the obtained PGA values range from 0.24 to 0.50 g (Figure 7d).

As expected, the highest values occur in the SW corner obviously due to the effects of the 6.14 magnitude seismic source 912 [63]. Outside this buffer zone the distribution of the PGA values is instead markedly correlated with the coefficient of lithological amplification and particularly the associated v_{s30} values therefore clustering around 0.24 and 0.33 g for type-*D* (v_{s30} < 180 m/s), and type-*C* (v_{s30} > 180 m/s) soils, respectively (Figure 7c).

Based on these PGA values and applying Equation (5), the probability of liquefaction in the Po delta plain was thus estimated. The obtained probabilities range from 0% to almost 17% and the compiled relevant map is represented in Figure 9. As expected, the probability distribution is obviously strongly influenced by the susceptibility of the outcropping units, but also by the different parameters of the tested seismic scenarios, especially the PGA.

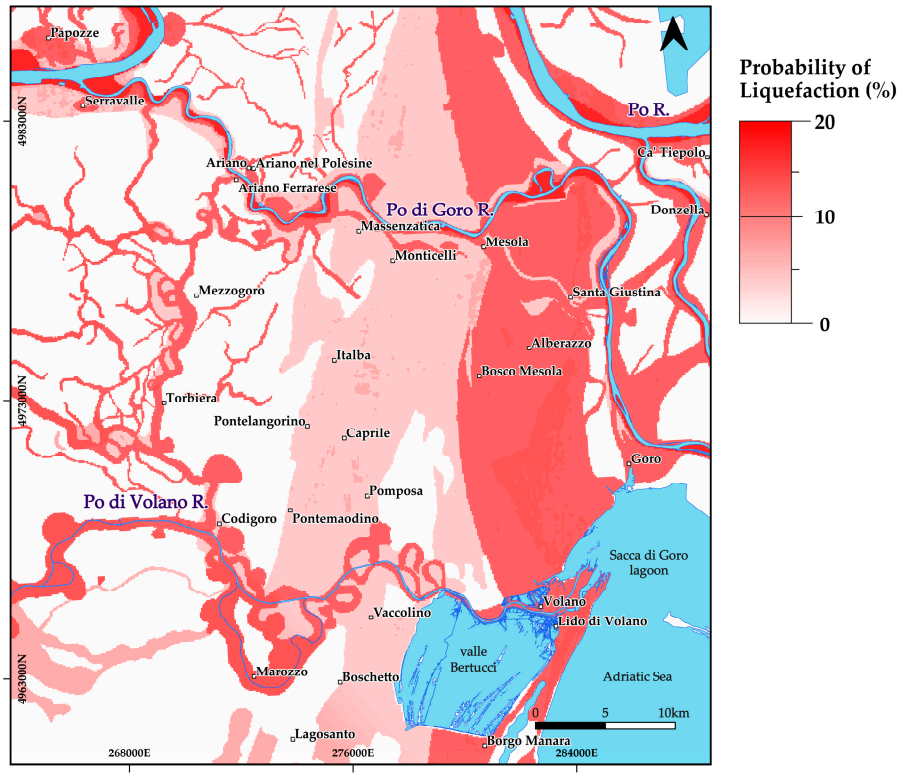


Figure 9. Map of the probability of liquefaction obtained in the present research by applying the HAZUS approach [73]. The names of the main urban centers are shown in black.

More specifically, the almost nul probability values prevail in the western sector of the map, where marsh deposits *m* are largely represented. Similar percentages characterize also the zones of brackish marshes and lagoons *sm* occurring in the eastern and locally central parts of the map. The beach barriers c_2 and the coastal dunes/beach ridges c_1 of the central longitudinal area result in higher probabilities of liquefaction, with values in the ranges 6–7% and 12–13% in the western (older) and eastern (younger) N–S trending strips, respectively. With a general west to east direction, the entire area is also crossed by several fluvial units. In particular, floodplain/deposits f_3 extending between the interdistributary plain and the abandoned channels a_3 show probability of liquefaction values of 4–7%, while the more recent floodplain/channels f_2, abandoned channels a_2 and crevasse splay bodies *cs* show even higher probabilities (12–13%).

Finally, in correspondence with the active floodplain f_1 of the major reaches of the Po River, crossing the northern sector of the investigated region, probability values up to almost 17% have been locally obtained.

4.3. Evaluation of Liquefaction Potential

Having assessed the liquefaction susceptibility of the surficial geological features, we additionally analyzed data derived from in situ tests, such as CPTu, randomly distributed within the studied area (Figure 6), and evaluated the corresponding *LPI* values. Specifically, the data were statistically analyzed using the box-and-whisker plot method and initially presented in groups according to liquefaction susceptibility classes, considering three distinct piezometric scenarios with groundwater table depths fixed at 0.5, 1.5, and 3.0 m below ground level.

Although in some sectors of the study area a groundwater depth of 0.5 m may represent a relatively uncommon condition relative to a seasonal average, at the current stage of the research a sufficiently dense and long-term piezometric monitoring network, representative

of each mapped geological unit, is not available. For this reason, it is not currently possible to quantitatively constrain or assign robust occurrence probabilities to the individual groundwater scenarios used in the *LPI* calculations. On the other hand, the results of the several models tested for calculating the probability of liquefaction (see Figure S3 in Supplementary Materials) indicate that deeper groundwater levels (down to 3.0 m) only slightly decrease (0.5–1%) the overall distribution obtained with the preferred input model and very locally up to 2% for the highest values in correspondence with the active floodplain f_1.

As shown in Figure 10, the *LPI* values at sites characterized as highly susceptible on a regional scale are higher than those of the other two classes, namely the moderate and non-susceptible to liquefaction classes. However, although the *LPI* values associated with the sites of the third group (i.e., non-susceptible to liquefaction) are clearly distinct from those of the other two for all groundwater-table scenarios, an overlap in *LPI* values can still be observed between the sites classified as susceptible to liquefaction.

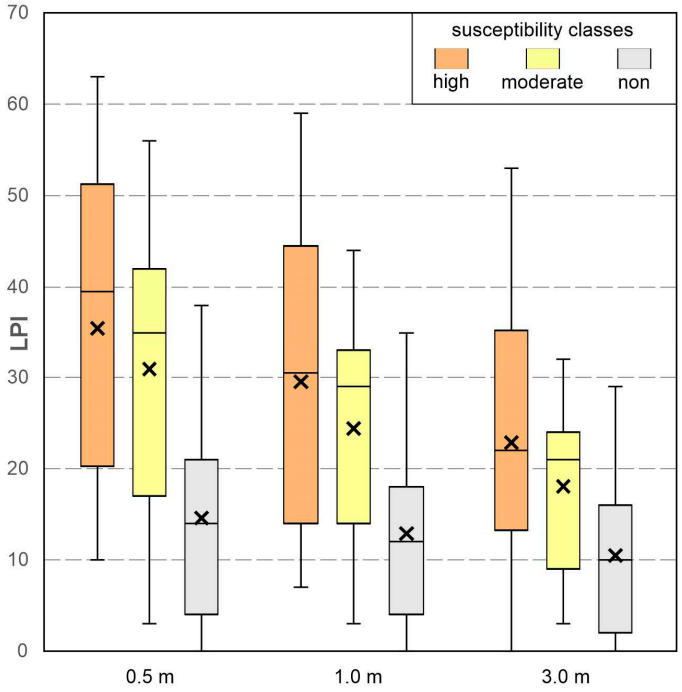


Figure 10. Whisker plots of the *LPI* values (vertical axis) obtained from CPTu carried out at sites within high (orange), moderate (yellow), and non-susceptible (gray) areas according to the regional scale (Figure 8) and calculated assuming water depths at 0.5, 1.0, and 3.0 m below the ground level (horizontal axis). x (symbol) is the median.

As expected, the *LPI* values at sites with the highest liquefaction susceptibility are also generally higher than those at moderately susceptible sites; however, it is not possible to define a clear threshold between these two classes for none of the three groundwater scenarios. Accordingly, the distribution of these values was further investigated by taking into account the type of deposits in which the in situ tests were performed. This analysis indicated that the deposits with the greatest liquefaction potential correspond to coastal dunes and beach ridges *c1*.

In addition, it is demonstrated that the average *LPI* value for each class systematically decreases as the groundwater table depth increases, confirming that a thicker non-liquefiable crust layer results in lower liquefaction potential at a site. Moreover, this decrease in *LPI* values is consistently observed across all susceptibility classes. This trend

highlights the importance of groundwater-level fluctuations in controlling liquefaction potential under varying geological and hydrogeological conditions.

4.3.1. Highly Liquefaction Susceptibility Areas

Regarding the features classified as highly susceptibility to liquefaction (Section 4.1), the average *LPI* values for a groundwater table depth equal to 0.5, 1.5, and 3.0 m are 29, 25, and 21 for the recent floodplain deposits *f2*; 43, 35, and 26 for coastal dunes/beach ridges *c1* and 27, 22, and 18 for deposits characterized as abandoned channels *a2* (Table 2 and Figure S4).

Table 2. High liquefaction susceptibility dataset: for each scenario of groundwater depth (m) the average *LPI* value calculated from available CPTu in the specified deposits and the corresponding weighted average at the 50th percentile are reported (n = number of CPTu. See also Table S2 and Figure S4 in Supplementary Materials (*c1*: more recent—<500 yr—coastal dunes/beach ridges).

Groundwater Depth (m)	II-Floodplain/Channels (*f2*) (n = 10)	Coastal Dunes/Beach Ridges (*c1*) (n = 15)	II-Abandoned Channels (*a2*) (n = 5)
	Average *LPI*		
0.5	29	43	27
1.5	25	35	22
3.0	21	26	18
weighted average on 50 percentiles			
0.5	22	42	55
1.5	20	36	47
3.0	17	28	35

Applying the box–whisker plot statistical analysis, for the same three groundwater depth scenarios it is possible to estimate that the weighted averages at the 50th percentile for floodplain deposits *f2* are 22, 20, and 17, with the highest and lowest *LPI* values (i.e., whisker) equal to 63, 59, and 53 and to 12, 11, and 6, respectively (Table 2 and Figure S4). For the case of more recent (<500 yr) coastal dunes/beach ridges *c1* the relevant values are 42, 36, and 28, while the outliers in terms of the highest and lowest *LPI* values are 55, 47, and 35 and 31, 28, and 22, respectively. Finally for the abandoned channels *a2* the weighted averages at the 50th percentile are 24, 12, and 14, while the highest and lowest values are 57, 53, and 43 and 10, 9, and 5, respectively.

4.3.2. Moderate Liquefaction Susceptibility Areas

As expected, the *LPI* values are generally lower for the CPTu carried out in deposits classified as moderate liquefaction susceptibility. Specifically, based on penetrometric tests on floodplain deposits *f3*, the averages are 24, 23, and 21 (for 0.5, 1.5, and 3.0 m depth of the water table, respectively; Table 3 and Figure S5), while on beach barriers *c2* the average *LPI* values are 26, 19 and 13.

It is worth noting that 13 out of 28 CPTu carried out in the 'older' Holocene coastal dunes/beach ridges *c1* (Table S1), have been classified as moderate susceptibility; however, this second group shows averages (40, 31 and 22) smaller than the former group, but slightly higher than the other coastal dunes/beach ridges deposits *c2*, which have been similarly classified as moderate. Finally, the average *LPI* values characterizing the abandoned channels *a3* are 9, 9, and 8 for the three-groundwater table related scenarios, respectively.

Table 3. Moderate liquefaction susceptibility dataset: for each scenario of groundwater depth (m) the average *LPI* value calculated from available CPTu in the specified deposits and the corresponding weighted average at the 50th percentile are reported (n = number of CPTu. See also Table S3 and Figure S5 in Supplementary Materials (*c1*: Holocene coastal dunes/beach ridges).

Groundwater Depth (m)	III-Floodplain/Channels (*f3*) (n = 2)	Beach Barriers (*c2*) (n = 4)	Coastal Dunes/Beach Ridges (*c1*) (n = 13)	III-Abandoned Channels (*a3*) (n = 4)
			Average *LPI*	
0.5	24	26	40	9
1.5	23	19	31	9
3.0	21	13	22	8
weighted average on 50 percentiles				
0.5		23	33	9
1.5		15	25	8
3.0		9	17	7

According to the outcome arisen by the box–whisker plot statistical analysis in the dataset of moderate susceptibility to liquefaction deposits (Table 3 and Figure S5), we estimated that the weighted averages at the 50th percentile for beach barriers *c2* are 23, 15, and 9 with the highest and lowest *LPI* values (i.e., whiskers) equal to 45, 35, and 24 and to 15, 12, and 9, respectively. For the cases of coastal dunes/beach ridges *c1* the relevant values are 33, 25 and 17, while the highest and lowest *LPI* values are equal to 50, 39 and 30 and to 22, 14 and 9, respectively. Finally, the abandoned channels *a3* are characterized by weighted averages at the 50th percentile equal to 9, 8, and 7 with highest and lowest *LPI* values equal to 17, 16, and 15 and 3, 3, and 3, respectively.

4.3.3. Non-Susceptible Liquefaction Areas

Finally, the non-susceptible to liquefaction class mainly consists of deposits described as marshes *m* and brackish marshes and lagoons *sm*. The average *LPI* values for the former are 17, 15, and 13 (for 0.5, 1.5, and 3.0 m depth respectively of water table; Table 4 and Figure S6) and systematically smaller for the latter ones (8, 7 and 5).

Table 4. Non-susceptible to susceptibility dataset: for each scenario of groundwater depth (m) is reported the average *LPI* value calculated from available CPTu in the specified deposits and the corresponding weighted average at the 50th percentile (n = number of CPTu. See also Table S4 and Figure S6 in Supplementary Materials).

Groundwater Depth (m)	Marshes (*m*) (n = 15)	Brackish Marshes and Lagoons (*sm*) (n = 5)
	Average *LPI*	
0.5	17	8
1.5	15	7
3.0	13	5
weighted average on 50 percentiles		
0.5	4	4
1.5	12	4
3.0	12	2

The whisker plots for this dataset reveal that the weighted averages at the 50th percentile for marshes are 14, 12, and 12, for the same groundwater scenarios, with the highest and lowest *LPI* values equal to 38, 35, and 29 and 4, 4, and 4, respectively. In case of lagoons *sm* deposits, the relevant values are 4, 4, and 2, while the highest and lowest *LPI* values are equal to 17, 14, and 10 and 2, 2, and 1, respectively (Table 4 and Figure S6).

5. Discussion

The results of the present study demonstrate a significant exposure of both critical infrastructure and the residential population in correspondence of areas characterized by moderate to high liquefaction susceptibility. Although the assessment is based on a regional scale mapping of the susceptibility classification, which inherently carries limitations in terms of spatial resolution and local soil variability, the findings of the present research provide a valuable first-order indication of where liquefaction induced hazards may be most likely to occur. Such information is essential for guiding future detailed investigations and for supporting risk-informed planning and decision-making.

5.1. Exposure of Critical Infrastructure and Population to Liquefaction Susceptibility

The integration of the liquefaction susceptibility map with infrastructure and demographic datasets (Figures 8 and 11) reveals a significant exposure of the study area to potential liquefaction effects. Indeed, a large proportion of the community is potentially exposed to liquefaction hazard, which could exacerbate the impact of seismic events on housing, services, and public safety. Out of approximately 47,600 inhabitants within the study area, and assuming a uniform distribution of the population within the urbanized areas, more than 70% reside in zones characterized by moderate-to-high liquefaction susceptibility. Specifically, about 10% of the urbanized areas are located in high susceptibility zones (e.g., Lido di Volano and Massa Fiscaglia). Approximately 33% live in areas of high-to-moderate susceptibility (e.g., Bosco Mesola and Taglio di Po). In addition, 28% of the inhabitants are situated in areas characterized by moderate-to-high susceptibility, such as Serravalle and Mesola. Moreover, buildings of historical and cultural interest, such as the Mesola Castle and the Abbey of Pomposa (Figure 1), are both located in areas characterized by high liquefaction susceptibility.

About 42% of the total length of the principal road network crossing the study area (SS309, SP16, and SR495) is located in areas characterized by high liquefaction susceptibility, whereas only 21% in sectors classified as non-susceptible. At this regard, liquefaction-induced settlement and/or lateral spreading could cause severe track misalignment, embankment failure, and prolonged service interruptions.

In particular, the road SS309 (Strada Romea), a major N–S transportation corridor connecting Ravenna to Venice, represents a strategic infrastructure with an average daily traffic volume of 149,486 vehicles (San Giuseppe di Comacchio monitoring station; Emilia-Romagna Region Transport Portal). Along this route, 37% of the path falls within areas of high liquefaction susceptibility, while the remaining 63% within areas of moderate susceptibility. Given its high traffic volume and national strategic role, even any minimal liquefaction-induced disruption along it could have a major impact for mobility and emergency response.

The railway network also exhibits a comparable level of exposure, with approximately 49% of the track alignment crossing areas of high liquefaction susceptibility, 27% within zones of moderate susceptibility, and only 24% in areas classified as non-susceptible. In addition, the railway stations of Massa Fiscaglia, Pomposa Zona Industriale, and Codigoro are located in areas classified as having high, moderate, and no susceptibility to liquefaction, respectively.

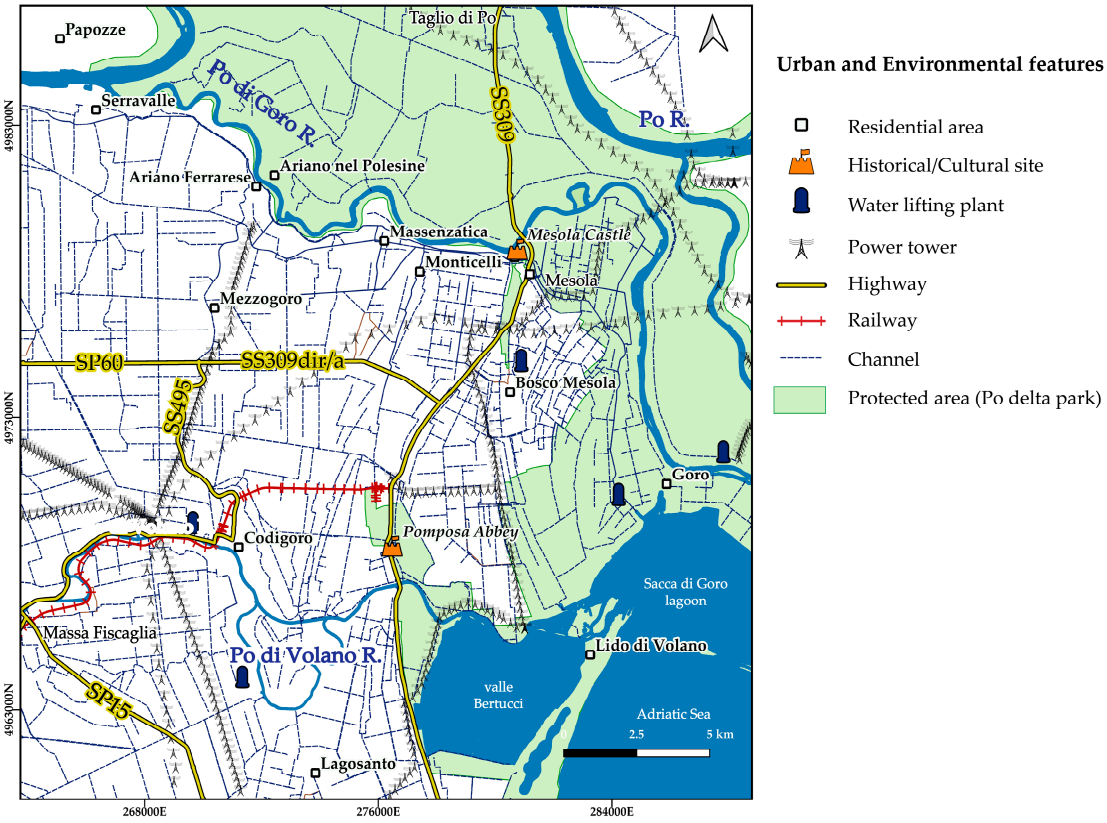


Figure 11. Main urban and environmental features of the investigated area (data based on a 1:50,000 scale topographic map).

Within the investigated area, 31% of the irrigation channels has been excavated across zones of high liquefaction susceptibility, 29% in zones of moderate susceptibility, and the remaining 40% in non-susceptible areas. Most important, all four pumping stations (hydraulic lift facilities) necessary for continuously draining the investigated area are positioned in high liquefaction susceptibility zones.

Finally, the analysis of power transmission infrastructures indicates that 24% of the 475 power towers stand in zones of high liquefaction susceptibility, 16% in areas of moderate, and the remaining 60% in non-susceptible zones.

5.2. Liquefaction Potential and Geomorphological Features

An additional and important issue to be addressed in liquefaction hazard analyses is the degree of reliability and precision of the available information relative to the liquefaction potential. In particular, one question that is often posed is how representative for a wider area is the value of the *LPI*, which is obtained at a specific site, and conversely which is the resolution of regional-scale maps obtained, for example, following the HAZUS [73] approach? In the frame of the present research, investigating alluvial and deltaic environments commonly characterized by lateral and vertical lithological heterogeneities even in correspondence of apparently uniform geomorphic features, these questions are of utmost importance.

As it has been shown in Section 4 (Results), the *LPI* values obtained at sites included in the same surficial geological unit could also vary significantly. The difference between the mean *LPI* value and the 50th percentile highlights the skewed distribution of the data, suggesting the influence of extreme values on the average and the greater representativeness of the median for describing typical liquefaction conditions. These conclusions represent a major outcome of the present study, indicating the importance of conducting in situ tests in

several locations also within the same geomorphological unit in order to compute more realistically the distribution of the liquefaction potential.

Moreover, the obtained results confirm that the complementary use of liquefaction susceptibility maps produced at a regional scale and site-specific (i.e., very local scale) analyses represents a crucial approach for more properly assessing this kind of natural hazard. Indeed, the former source of information (i.e., regional scale map) delineates areas more or less prone to liquefaction on the basis surficial geological mapping and geomorphological analyses. The latter source of information (i.e., CPTu) is instead quantitative in estimating the liquefaction potential settlement (i.e., *LPI*) but limited to the sites where the in situ test is carried out.

At this regard, Figure 12 shows representative examples of lithological successions obtained from the analysis of CPTu data at sites classified as high (A, B, C), moderate (D, E, F) and non-susceptible (G, H) to liquefaction, respectively. It is worth noting that the lithological successions obtained from the penetrometric tests could largely vary within the same class of potential liquefaction or be similar at sites characterized by two different classes. For example, though the A, B, and C sites (Figure 12) have been classified as high susceptibility to liquefaction, the corresponding CPTu have been performed in distinct mapped units, namely the floodplain deposits *f2*, the coastal dunes *c1* and the abandoned channels *a2*, respectively.

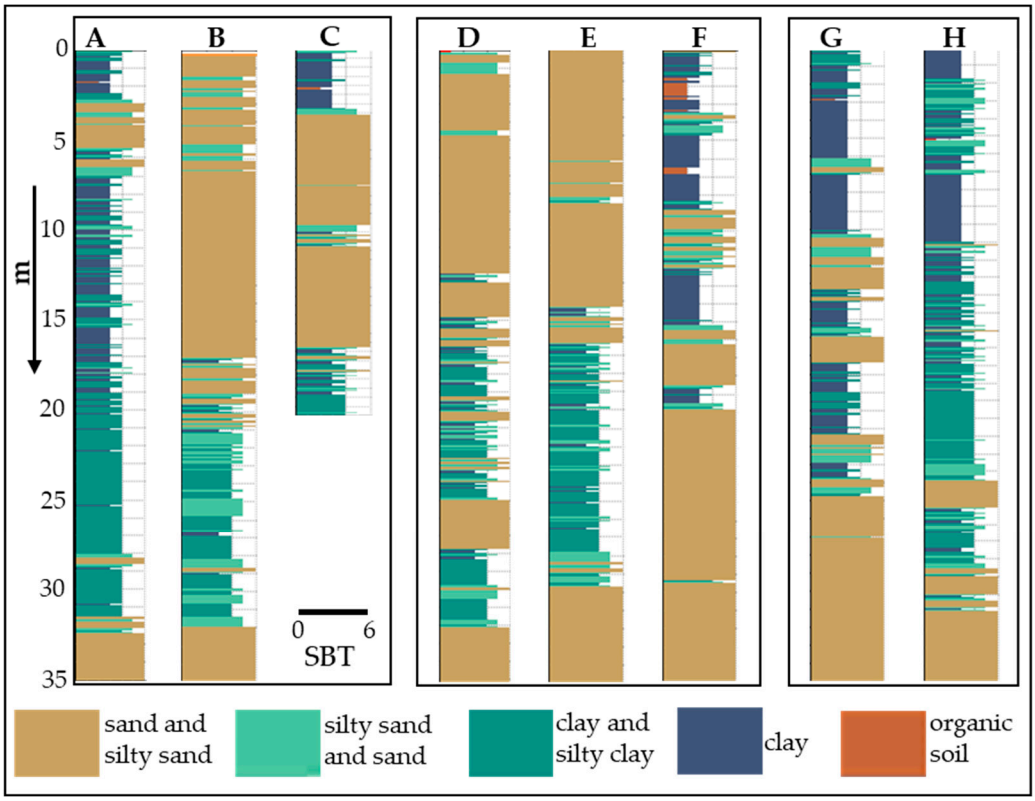


Figure 12. Examples of underground lithological sequences (depth in meters) as they were obtained from CPTu data processing in CLiq software. SBT is the Soil Behavior Type Index proposed by Robertson and Wride [78]. CPTu with high susceptibility to liquefaction were carried out in floodplain deposits *f2* (**A**), coastal dunes *c1* (**B**) and abandoned channels *a2* (**C**); CPTu in moderate susceptibility to liquefaction were carried out in beach barriers *c2* (**D**), coastal dunes/beach ridges *c1* (**E**), and abandoned channels *a3* (**F**). CPTu in non-susceptibility to liquefaction were carried out in marshes *m* (**G**) and brackish marshes and lagoons *sm* (**H**). For the corresponding locations see Figure 8.

In particular, though the behavior at the three sites is expected to be similar relative to soil liquefaction, the subsoil stratigraphies significantly differ: the floodplain deposits *f2* are characterized by highly stratified soil layers dominated by finer material (i.e., silt and clay), the coastal dunes *c1* subsoil stratigraphy is characterized by a major sandy layer alternating with thin (less than 1 m-thick) silty material, while the abandoned channel *a2* site is characterized by a surficial clay-like material (up to a depth of 3 m) that overlays a thick sandy level.

In principle, solely based on the penetrometric data provided by in situ tests, floodplain deposits *f2* should be not capable of inducing severe liquefaction. However, the occurrence of sand-silty sand and relatively thin layers at shallow depth may possibly generate small-size liquefaction phenomena. Accordingly, considering this geological setting and depositional unit as highly susceptible to liquefaction represents a conservative scenario.

Relative to the geological units classified as moderate susceptibility to liquefaction (Figure 12), we selected three subsoil stratigraphic logs (D, E, F) representative of the beach barriers *c2*, the coastal dunes/beach ridges *c1*, and the abandoned channels *a3*. As expected, in correspondence of the beach barriers and ridges (units *c1* and *c2*) most of the shallow (up to 10–15 m) sedimentary succession is represented by sand with only a few thin layers of silty sand, like the one encountered in the same unit but classified as high susceptibility (B). On the other hand, the geomorphological feature of abandoned channels (F) is highly stratified showing clay and silty layers of less than 1 m-thick at the surface covering coarser layers. According to Hutabarat and Bray [80], this highly stratified succession is not expected to produce large amount of ejecta and consequently the classification of these deposits as moderate susceptible to liquefaction may be considered quite conservative. Nevertheless, the contradiction between the site classification obtained on the basis of a regional-scale approach and the site-specific scale results obtained from penetrometric tests confirms the need for the urban environments of conducting in situ tests for more properly and accurately evaluating the liquefaction potential.

Finally, regarding the deposits classified as non-susceptible to liquefaction (Figure 12), the local-scale information derived from CPTu data agrees with the characterization at the regional scale. As can be seen in logs G and H (Figure 12), both units (marshes *m* and brackish marshes and lagoons *sm*) mainly consist of clay-rich soils dominated also at shallow depth by clay layers. Typically, these soils are considered non-susceptible to liquefaction either at the regional and site-specific scales. In this case, the detailed subsoil stratigraphy obtained from the penetrometric tests confirms the classification on regional scale. However, the outliers of *LPI* values described in the Results section, suggest that cases of high liquefaction potential could not be excluded.

This contradiction may be due to the 1:50,000 mapping scale compared to the 1:500 local scale and/or to the specific laterally variable depositional conditions being not feasible distinguishing them on a regional-scale map. In order to overcome this issue, it is suggested to perform a few randomly distributed in situ tests to verify or update the outcome of a regional-scale approach, which in turn provides a general view of the liquefaction hazard distribution. Adopting a transect-based reporting framework, in which CPTu-derived *LPI* values are presented along systematic profiles rather than as scattered point estimates within unit polygons, would also bring the present approach closer to recent best practice in multi-decadal coastal-vulnerability work [81,82] and would make the regional-to-local handoff more transparent for non-specialist users of the map.

6. Conclusions

Liquefaction during earthquakes is strongly influenced by the depositional history, including sediment type, age, shallow layering, and groundwater depth. Holocene, un-

consolidated sediments, particularly in (palaeo-)channels and coastal point bars, are more susceptible than other deposits.

The accuracy of susceptibility maps depends on the scale of investigation and the quality and density of geological, geomorphological, and hydrogeological data. This research focuses on a 560 km^2 area in the eastern sector of the Po River Plain (northern Italy), encompassing part of the modern Po Delta, to assess the liquefaction susceptibility of local geological units. A comprehensive dataset was used, including lithological, chronological (^{14}C), geomorphological, hydrological, and hydrogeological information, as well as satellite imagery, historical and modern maps, archaeological evidence, and subsurface data from core drilling and penetrometer tests. The integrated data analysis allowed to define the liquefaction susceptibility map at the regional scale following the HAZUS approach and distinguishing the outcropping units into four classes, corresponding to the following susceptibility levels:

(a) very high, in the portion of the territory occupied by the floodplain of the principal reach of the Po channel, which accounts for 4% of the area;
(b) high, corresponding to 26% of the area, characterizing geological formations such as floodplains, channels, crevasse splays, abandoned channels, and coastal dunes;
(c) moderate, covering approximately 20% of the territory, mainly in correspondence of beach barrier deposits;
(d) non-susceptible to liquefaction, representing 50% of the territory, including marshes of interdistributary areas and brackish marshes and lagoons of the front delta plain, dominated by clays, silty clays, and silts.

In parallel, CPTu data collected across different lithological units have been statistically analyzed (see Section 4.3) in terms of Liquefaction Potential Index (*LPI*). A detailed analysis of the *LPI* values for sites classified as high, moderate, and low susceptibility, under three groundwater table scenarios (0.5, 1.5, and 3.0 m), generally indicates a decrease in *LPI* with increasing groundwater depth, an increase of the *LPI* with increasing susceptibility classes (from non-susceptible to high susceptibility), but also a significant variability within the same surficial geological unit due to vertical and lateral heterogeneity.

Discrepancies between regional-scale susceptibility maps and site-specific investigations highlight the importance of integrating both approaches to accurately assess liquefaction risk and guide mitigation strategies.

Furthermore, the analysis shows that critical infrastructure and residential populations within the study area are substantially exposed to zones of moderate to high liquefaction susceptibility. Although regional-scale mapping has inherent limitations in spatial resolution and soil variability, it provides a valuable first-order assessment for identifying areas most likely affected by liquefaction, supporting future detailed investigations and risk-informed planning.

Finally, this study aims to contribute to the understanding of liquefaction susceptibility in urbanized areas characterized by complex depositional environments—specifically alluvial and deltaic plains—and the presence of aquifers with water table fluctuations ranging from 0.5 to 3.0 m below ground level.

Supplementary Materials: The following supporting information can be downloaded at: https://www.mdpi.com/article/10.3390/environments13060343/s1, Table S1. Age and corresponding geological unit of the dated samples (for their location, see Figure 3; Servizio Geologico d'Italia, 2009). Table S2. LPI values computed based on CPTu carried out on high liquefaction susceptibility areas. Numbers in bold represent the average LPI value for each groundwater depth scenario. Table S3. LPI values computed based on CPTu carried out on moderate liquefaction susceptibility areas. Numbers in bold represent the average LPI value for each groundwater depth scenario. Table S4. LPI values

computed based on CPTu carried out on non-susceptible to liquefaction areas. Numbers in bold represent the average LPI value for each groundwater depth scenario. Figure S1. PGA distribution for some of the tested double gradient seismic input models assuming a NNE-wards focal depth decrease from 8 to 6 km and a magnitude reduction of 0.02 (a), 0.03 (b), 0.05 (c), and 0.07 (d) M_w units per kilometre of distance from the border of the 912 zone starting from M = 6.14 and considering the centroid of each mesh as a potential epicenter. Figure S2. PGA distribution for the seismic input models assuming each mesh is the source of a magnitude of 5.0 at different focal depths corresponding to 6 (a), 7 (b), and 8 (c) km, while in (d) it is assumed a unique focus at the SW corner for a 6.14 magnitude event. Figure S3. Some of the tests performed to verify the effect of different groundwater levels on the probability of liquefaction. The assumed water depth is 0.5 and 3.0 m in the left and right columns, respectively, for a double-gradient model (a,b), a fixed-depth and fixed-magnitude model (c,d), and for the composite preferred model (e,f). Figure S4. High liquefaction susceptibility areas: weighted average on 50 percentiles for each scenario of groundwater depth (m). Figure S5. Moderate liquefaction susceptibility areas: weighted average on 50 percentiles for each scenario of groundwater depth (m). Figure S6. Non-susceptible to liquefaction areas: weighted average on 50 percentiles for each scenario of groundwater depth (m).

Author Contributions: Conceptualization, D.R.; methodology, D.R. and G.P.; software, D.R., G.P., M.T., and R.C.; validation, D.R. and G.P.; formal analysis, D.R., G.P., M.T., and R.C.; investigation, D.R., R.C., and G.P.; resources, D.R. and R.C.; data curation D.R., R.C., and G.P.; writing—original draft preparation, D.R., G.P., M.T., and R.C.; writing—review and editing, D.R. and G.P.; visualization, D.R. and G.P.; supervision, D.R.; project administration, D.R.; funding acquisition, R.C. All authors have read and agreed to the published version of the manuscript.

Funding: The research activities of G.P. was partially supported by the H.F.R.I ("3rd Call for H.F.R.I.'s Research Projects to Support Faculty Members & Researchers" Project Number: 25030).

Data Availability Statement: The data presented in this study are available on request from the corresponding author due to privacy restrictions.

Acknowledgments: We thank Regione Emilia-Romagna for providing geological data. We also thank the anonymous reviewers for their constructive comments, which improved the manuscript.

Conflicts of Interest: Author Dimitra Rapti was employed by the company New Energies And environment—NEA Ltd. The remaining authors declare that the research was conducted in the absence of any commercial or financial relationships that could be construed as a potential conflict of interest.

References

1. Zeybek, A.; Madabhushi, S.P.G. Influence of air injection on the liquefaction-induced deformation mechanisms beneath shallow foundations. *Soil Dyn. Earthq. Eng.* **2017**, *97*, 266–276. [CrossRef]
2. Marasini, N.P.; Okamura, M. Numerical simulation of centrifuge tests to evaluate the performance of desaturation by air injection on liquefiable foundation soil of light structures. *Soils Found.* **2015**, *55*, 1388–1399. [CrossRef]
3. Mahmoud, A.O.; Hussien, M.N.; Karray, M.; Chekired, M.; Bessette, C.; Jinga, L. Mitigation of liquefaction-induced uplift of underground structures. *Comput. Geotech.* **2020**, *125*, 103663. [CrossRef]
4. Rogers, N.; Williams, K.; Jacka, M.; Wallace, S.; Leeves, J. Geotechnical aspects of disaster recovery planning in residential Christchurch and surrounding districts affected by liquefaction. *Earthq. Spectra* **2014**, *30*, 493–512. [CrossRef]
5. Van Ballegooy, S.; Wentz, F.; Boulanger, R.W. Evaluation of CPT-based liquefaction procedures at regional scale. *Soil Dyn. Earthq. Eng.* **2015**, *79*, 315–334. [CrossRef]
6. Potter, S.H.; Becker, J.S.; Johnston, D.M.; Rossiter, K.P. An overview of the impacts of the 2010–2011 Canterbury earthquakes. *Int. J. Disaster Risk Reduct.* **2015**, *14*, 6–14. [CrossRef]
7. King, A.; Middleton, D.; Brown, C.; Johnston, D.; Johal, S. Insurance: Its role in recovery from the 2010–2011 Canterbury Earthquake sequence. *Earthq. Spectra* **2014**, *30*, 475–491. [CrossRef]
8. Holzer, T.L. (Ed.) *The Loma Prieta, California, Earthquake of October 17, 1989: Strong Ground Motion and Ground Failure*; U.S. Geological Survey Professional Paper 1551; United States Government Printing Office: Washington, DC, USA, 1992.

9. O'rourke, T.D. An Overview of Geotechnical and Lifeline Earthquake Engineering. In *Geotechnical Earthquake Engineering and Soil Dynamics III*; ASCE Publication: Reston, VA, USA, 1998; pp. 1392–1426.
10. Bray, J.D.; Sancio, R.B.; Kammerer, A.M.; Merry, S.; Rodriguez-Marek, A.; Khazai, B.; Chang, S.; Bastani, A.; Collins, B.; Hausler, E.L.; et al. Some Observations of Geotechnical Aspects of the February 28, 2001 Nisqually Earthquake in Olympia, South Seattle, and Tacoma, Washington. GEER Association Report No. GEER-005. 2001. Available online: https://apps.peer.berkeley.edu/publications/nisqually/geotech/index.html (accessed on 1 June 2026).
11. Horspool, N.A.; King, A.B.; Lin, S.L.; Uma, S.R. Damage and losses to residential buildings during the Canterbury earthquake sequence. In Proceedings of the 2016 New Zealand Society for Earthquake Engineering, Christchurch, New Zealand, 1–3 April 2016.
12. Cubrinovski, M.; Bray, J.D.; Taylor, M.; Giorgini, S.; Bradley, B.; Wotherspoo, L.; Zupan, J. Soil liquefaction effects in the Central Business District during the February 2011 Christchurch earthquake. *Seismol. Res. Lett.* **2011**, *82*, 893–904. [CrossRef]
13. Bahari, B.; Hwang, W.; Kim, T.H.; Song, Y.S. Estimation of liquefaction potential in Eco-Delta City (Busan) using different approaches with effect of fines content. *Int. J. Geo-Eng.* **2020**, *11*, 14. [CrossRef]
14. Niu, J.; Xie, J.; Lin, S.; Lin, P.; Gao, F.; Zhang, J.; Cai, S. Importance of bed liquefaction-induced erosion during the winter wind storm in the Yellow River Delta, China. *J. Geophys. Res. Ocean.* **2023**, *128*, e2022JC019256. [CrossRef]
15. Kamal, A.M.M.; Sahebi, M.T.; Hossain, M.S.; Rahman, M.Z.; Fahim, A.K.F. Liquefaction hazard mapping of the south-central coastal areas of Bangladesh. *Nat. Hazards Res.* **2024**, *4*, 520–529. [CrossRef]
16. Sun, H.; Xu, J.; Tian, Z.; Qiao, L.; Luan, Z.; Zhang, Y.; Zhang, S.; Liu, X.; Li, G. Seabed liquefaction risk assessment based on wave spectrum characteristics: A case study of the Yellow River Subaqueous Delta, China. *J. Mar. Sci. Eng.* **2024**, *12*, 2276. [CrossRef]
17. Youd, T.L.; Perkins, D.M. Mapping of Liquefaction induced Ground Failure Potential. *J. Geotech. Eng. Div.* **1978**, *104*, 433–446. [CrossRef]
18. Wakamatsu, K. *Evaluation of Liquefaction Susceptibility Based on Detailed Geomorphological Classification, Proceedings of the Annual Meeting of the Architectural Institute of Japan*; Architectural Institute of Japan (AIJ): Tokyo, Japan, 1992; pp. 1443–1444.
19. Wakamatsu, K.; Yamamoto, A.; Tanaka, I. Geomorphological criteria for evaluating liquefaction potential considering the level-2 ground motion in Japan. In Proceedings of the 4th International Conference Recent Advances in Geotechnical Earthquake Engineering and Soil Dynamics, San Diego, CA, USA, 29 March 2001; pp. 26–31.
20. Youd, T.L.; Hoose, S.N. *Historic Ground Failures in Northern California Associated with Earthquakes*; Professional Paper 993; U.S. Geological Survey: Reston, VA, USA, 1978.
21. Steinbrugge, K.V.; Moran, D.F. Damage caused by the earthquake of July 6 and August 23, 1954. *Bull. Seism. Soc. Am.* **1956**, *46*, 15–33. [CrossRef]
22. Kachadoorian, R. *Effects of the Earthquake of 27 March 1964, on Alaska Highway System*; Professional Paper 545-C; U.S. Geological Survey: Reston, VA, USA, 1968.
23. Ferrians, O.J. *Effects of Earthquake of 27 March 1964, in Cooper River Basin Area, Alaska*; Professional Paper 543-E; U.S. Geological Survey: Reston, VA, USA, 1966. [CrossRef]
24. Kuribayashi, E.; Tatsuoka, F. Brief review of liquefaction during earthquakes in Japan. *Soils Found.* **1975**, *15*, 81–92. [CrossRef] [PubMed]
25. Wotherspoon, L.; Pender, M.; Orense, R.P. Relationship between observed liquefaction at Kaiapoi following the 2010 Darfield earthquake and former channels of the Waimakariri River. *Eng. Geol.* **2012**, *125*, 45–55. [CrossRef]
26. Di Manna, P.; Guerrieri, L.; Piccardi, L.; Vittori, E.; Castaldini, D.; Berlusconi, A.; Bonadeo, L.; Comerci, V.; Ferrario, F.; Gambillara, R.; et al. Ground effects induced by the 2012 seismic sequence in Emilia: Implications for seismic hazard assessment in the Po Plain. *Ann. Geophys.* **2012**, *55*, 697–703. [CrossRef]
27. Bastin, S.; Quigley, M.; Bassett, K. Paleoliquefaction in eastern Christchurch, New Zealand. *Geol. Soc. Am. Bull.* **2015**, *12*, 1348–1365. [CrossRef]
28. Bastin, S.; Stringer, M.; Green, R.; Wotherspoon, L.; van Ballegooy, S.; Cox, B.; Osuchowski, A. Geomorphological controls on the distribution of liquefaction in Blenheim, New Zealand, during the 2016 Mw7.8 Kaikoura Earthquake. In *Geotechnical Earthquake Engineering and Soil Dynamics V: Liquefaction Triggering, Consequences, and Mitigation*; GSP 290; The American Society of Civil Engineers (ASCE): Reston, VA, USA, 2018.
29. Papathanassiou, G.; Caputo, R.; Rapti-Caputo, D. Liquefaction phenomena along the paleo-Reno River caused by the May 20, 2012, Emilia (northern Italy) earthquake. *Ann. Geophys.* **2012**, *55*, 735–742. [CrossRef]
30. Papathanassiou, G.; Mantovani, A.; Tarabusi, G.; Rapti, D.; Caputo, R. Assessment of liquefaction potential for two liquefaction prone area considering the May 20, 2012 Emilia (Italy) earthquake. *Eng. Geol.* **2015**, *189*, 1–16. [CrossRef]
31. Papathanassiou, G.; Valkaniotis, S.; Ganas, A.; Stampolidis, A.; Rapti, D.; Caputo, R. Floodplain evolution and its influence on liquefaction clustering: The case study of March 2021 Thessaly, Greece, seismic sequence. *Eng. Geol.* **2022**, *298*, 106542. [CrossRef]

32. Civico, R.; Brunori, C.A.; De Martini, P.M.; Pucci, S.; Cinti, F.R.; Pantosti, D. Liquefaction susceptibility assessment in fluvial plains using airborne lidar: The case of the 2012 Emilia earthquake sequence area (Italy). *Nat. Hazard Earth Syst. Sci.* **2015**, *15*, 2473–2483. [CrossRef]
33. Taftsoglou, M.; Valkaniotis, S.; Karantanellis, S.; Goula, E.; Papathanassiou, G. Preliminary mapping of liquefaction phenomena triggered by the February 6 2023 M7.7 earthquake, Türkiye/Syria, based on remote sensing data. *Zenodo* **2023**, *preprint*. [CrossRef]
34. Abayo, I.; Caba, A.; Chamberlin, E.; Montoya, B. Fluvial geomorphic factors affecting liquefaction-induced lateral spreading. *Earthq. Spectra* **2023**, *39*, 2518–2547. [CrossRef]
35. Zhang, H.; Lu, Y.; Liu, X.; Li, X.; Wang, Z.; Ji, C.; Zhang, C.; Wang, Z.; Jing, S.; Jia, Y. Morphology and origin of liquefaction-related sediment failures on the Yellow River subaqueous delta. *Mar. Pet. Geol.* **2023**, *153*, 106262. [CrossRef]
36. Qin, X.; Yang, Z.; Cui, Y.; Liu, X.; Tian, H.; Guo, L.; Ling, X. Spatial distribution characteristics of soil liquefaction potential in the Yellow River Subaquatic Delta, China. *Mar. Georesour. Geotechnol.* **2024**, *42*, 420–431. [CrossRef]
37. Dudley Ward, N.F. On the mechanism of earthquake induced groundwater flow. *J. Hydrol.* **2015**, *530*, 561–567. [CrossRef]
38. Widodo, L.E.; Prassetyo, S.H.; Simangunsong, G.M.; Iskandar, I. Role of the confined aquifer in the mechanism of soil liquefaction due to the 7.5 Mw earthquake in Palu (Indonesia) on 28 September 2018. *Hydrogeol. J.* **2022**, *30*, 1877–1898. [CrossRef]
39. Chang, M.; Chan, M.S.; Huang, R.C.; Upomo, T.C.; Kusumawardani, R. Assignment of Groundwater Table in Liquefaction Analysis of Soils. In *Advancements in Geotechnical Engineering. Sustainable Civil Infrastructures*; Shehata, H., Badr, M., Eds.; Springer International Publishing: Cham, Switzerland, 2021; pp. 3–18. [CrossRef]
40. Dinastiyanto, T.; Hardiyatmo, H.C.; Pratiwi, E.P.A. Liquefaction potential analysis of irrigation canals at Sidera area-Sigi Regency. In *IOP Conference Series: Earth and Environmental Science, Proceedings of the International Conference on Geological Engineering and Geosciences., Yogyakarta, Indonesia, 21–22 September 2023*; IOP Publishing Ltd.: Bristol, UK, 2023; Volume 1373. [CrossRef]
41. Liu, C.Y.; Chia, Y.; Chuang, P.Y.; Chiu, Y.C.; Tseng, T.L. Impacts of hydrogeological characteristics on groundwater level changes induced by earthquakes. *Hydrogeol. J.* **2018**, *26*, 451–465. [CrossRef]
42. Elkhoury, J.E.; Brodsky, E.E.; Agnew, D.C. Seismic waves increase permeability. *Nature* **2006**, *411*, 1135–1138. [CrossRef] [PubMed]
43. Bradley, K.; Mallick, R.; Andikagumi, H.; Hubbard, J.; Meilianda, E.; Switzer, A.; Du, N.; Brocard, G.; Alfian, D.; Benazir, B.; et al. Earthquake-triggered 2018 Palu Valley landslides enabled by wet rice cultivation. *Nat. Geosci.* **2019**, *12*, 935–939. [CrossRef]
44. Cox, S.C.; van Ballegooy, S.; Rutter, H.K.; Harte, D.S.; Holden, C.; Gulley, A.K.; Lacrosse, V.; Manga, M. Can artesian groundwater and earthquake-induced aquifer leakage exacerbate the manifestation of liquefaction? *Eng. Geol.* **2021**, *281*, 105982. [CrossRef]
45. United Nations. *Transforming Our World: The 2030 Agenda for Sustainable Development*; United Nations: New York, NY, USA, 2015; Available online: https://sdgs.un.org/2030agenda (accessed on 1 June 2026).
46. Pieri, M.; Groppi, G. *Subsurface Geological Structure of the Po Plain, Italy*; Progetto Finalizzato Geodinamica, Sottoprogetto Modello Strutturale, Publication N° 414; Consiglio Nazionale delle Ricerche: Roma, Italy, 1981; p. 23.
47. Regione Emilia-Romagna ENI-AGIP. *Riserve Idriche Sotterranee Della Regione Emilia-Romagna*; Di Dio, G., Ed.; S.EL.CA.: Florence, Italy, 1998; 120p.
48. Toscani, G.; Burrato, P.; Di Bucci, D.; Seno, S.; Valensise, G. Plio-Quaternary tectonic evolution of the Northern Apennines thrust fronts (Bologna-Ferrara section, Italy): Seismotectonic implications. *Boll. Soc. Geol. It.* **2009**, *128*, 605–613. [CrossRef]
49. Caputo, M.; Pieri, L.; Unguendoli, M. Geometric investigations of the subsidence in the Po delta. *Boll. Geofis. Teor. Appl.* **1970**, *13*, 187–207.
50. Ciabatti, M. Geomorfologia ed evoluzione del Delta Padano. In *Il Mondo Della Natura in Emilia-Romagna: La Pianura e la Costa*; Amilcare Pizzi: Cinisello Balsamo, Italy, 1990; pp. 9–18.
51. Bondesan, M. *Nuovi Dati Sull'evoluzione Dell'antico Delta Padano in Epoca Storica*; Atti della Accademia Delle Scienze di Ferrara; XLIII-XLIV (1965–1967); Industrie Grafiche: Ferrara, Italy, 1968; pp. 1–16.
52. Bondesan, M.; Bucci, V. The Ancient Coastal Ridges of the South-Western Sector of the Comacchio Valleys. *Atti Della Accad. Delle Sci. Ferrara* **1972**, *48*, 1–18. (In Italian)
53. Fabbri, P. Coastline variations in the Po delta since 2500 BP in Geomorphology of changing coastlines. *Z. Für Geomorphol.* **1985**, *57*, 155–167.
54. Fabbri, P. *Le Trasformazioni Della Costa Tra il Po e l'Appennino Sulla Base Della Documentazione Cartografica D'età Moderna*; Collana di Studi sul Territorio; Dipartimento di Geografia e Geologia Ambientale: Bologna, Italy, 1994; pp. 1–129.
55. Veggiani, A. Il deterioramento climatico dei Secoli XVI-XVIII ed i suoi effetti sulla bassa Romagna. *Studi Romagnoli* **1984**, *35*, 109–124.
56. Servizio Geologico D'Italia. *Carta Geologica D'Italia Alla Scala 1:50,000, Foglio 187 Codigoro*; ISPRA: Roma, Italy, 2009. [CrossRef] [PubMed]
57. Rapti-Caputo, D.; Martinelli, G. The geochemical and isotopic composition of aquifer systems in the deltaic region of the Po River plain (northern Italy). *Hydrogeol. J.* **2009**, *17*, 467–480. [CrossRef]

58. Marrocchino, E.; Rapti-Caputo, D.; Vaccaro, C. Chemical-mineralogical characterisation as useful tool in the assessment of the decay of the Mesola Castle (Ferrara, Italy). *Constr. Build. Mater.* **2010**, *24*, 2672–2683. [CrossRef]
59. Rapti, D.; Martinelli, G. An Expedited Procedure to Highlight Rapid Recharge Processes by Means of Nitrate Pollution Dynamics in the Northern Italy Plain. *Environments* **2025**, *12*, 404. [CrossRef]
60. Amorosi, A.; Bruno, L.; Campo, B.; Morelli, A.; Rossi, V.; Scarponi, D.; Hong, W.; Bohacs, K.M.; Drexler, T.M. Global sea-level control on local parasequence architecture from the Holocene record of the Po Plain, Italy. *Mar. Petrol. Geol.* **2017**, *87*, 99–111. [CrossRef]
61. Youd, T.L. *Screening Guide for Rapid Assessment of Liquefaction Hazard at Highway Bridge Sites*; Technical Report MCEER-98-0005; Multidisciplinary Center for Earthquake Engineering Research (U.S.): New York, NY, USA, 1998; p. 58.
62. Valkaniotis, S.; Rapti, D.; Taftsoglou, M.; Papathanassiou, G.; Caputo, R. Geomorphological mapping for liquefaction likelihood: The Piniada Valley case study (central Greece). *Bull. Earthq. Eng.* **2024**, *22*, 5451–5474. [CrossRef]
63. Meletti, C.; Valensise, G. Zonazione sismogenetica ZS9. Appendice 2. In *Redazione della Mappa di Pericolosità Sismica Prevista Dall'ordinanza PCM 3274 del 20 Marzo 2003, Rapporto Conclusivo per il Dipartimento della Protezione Civile*; INGV: Roma, Italy, 2004; 65p.
64. Castelli, V.; Bernardini, F.; Camassi, R.; Caracciolo, C.H.; Ercolani, E.; Postpischl, L. Looking for missing earthquake traces in the Ferrara–Modena plain: An update on historical seismicity. *Ann. Geophys.* **2012**, *55*, 519–524. [CrossRef]
65. Rovida, A.; Locati, M.; Camassi, R.; Lolli, B.; Gasperini, P. *Catalogo Parametrico dei Terremoti Italiani (CPTI15)*, version 2.0; Istituto Nazionale di Geofisica e Vulcanologia (INGV): Rome, Italy, 2019. [CrossRef]
66. Rovida, A.; Locati, M.; Camassi, R.; Lolli, B.; Gasperini, P. The Italian earthquake catalogue CPTI15. *Bull. Earthq. Eng.* **2020**, *18*, 2953–2984. [CrossRef]
67. Pondrelli, S.; Salimbeni, S.; Perfetti, P.; Danecek, P. Quick regional centroid moment tensor solutions for the Emilia 2012 (northern Italy) seismic sequence. *Ann. Geophys.* **2012**, *55*, 615–621. [CrossRef]
68. Bindi, D.; Pacor, F.; Luzi, L.; Puglia, R.; Massa, M.; Ameri, G.; Paolucci, R. Ground motion prediction equations derived from the Italian strong motion database. *Bull. Earthq. Eng.* **2011**, *9*, 1899–1920. [CrossRef]
69. Norini, G.; Aghib, F.S.; Di Capua, A.; Facciorusso, J.; Castaldini, D.; Marchetti, M.; Cavallin, A.; Pini, R.; Ravazzi, C.; Zuluaga, M.C.; et al. Assessment of liquefaction potential in the central Po plain from integrated geomorphological, stratigraphic and geotechnical analysis. *Eng. Geol.* **2021**, *282*, 105997. [CrossRef]
70. Mori, F.; Mendicelli, A.; Moscatelli, M.; Romagnoli, G.; Peronace, E.; Naso, G. A new Vs30 map for Italy based on the seismic microzonation dataset. *Eng. Geol.* **2020**, *275*, 105745. [CrossRef]
71. Masetti, D.; Fantoni, R.; Romano, R.; Sartorio, D.; Trevisani, E. Tectonostratigraphic evolution of the Jurassic extensional basins of the eastern southern Alps and Adriatic foreland based on an integrated study of surface and subsurface data. *Am. Ass. Petrol. Geol. Bull.* **2012**, *96*, 2065–2089. [CrossRef]
72. Meletti, C.; Galadini, F.; Valensise, G.; Stucchi, M.; Basili, R.; Barba, S.; Vannucci, G.; Boschi, E. A seismic source zone model for the seismic hazard assessment of the Italian territory. *Tectonophysics* **2008**, *450*, 85–108. [CrossRef]
73. FEMA (Federal Emergency Management Agency). *Hazus Earthquake Model Technical Manual*; Hazus 5.1; FEMA: Washington, DC, USA, 2022.
74. Liao, S.S.C.; Veneziano, D.; Whitman, R.V. Regression models for evaluating liquefaction probability. *J. Geotech. Eng.* **1988**, *114*, 389–411. [CrossRef]
75. Iwasaki, T.; Tatsuoka, F.; Tokida, K.; Yasuda, S. A practical method for assessing soil liquefaction potential based on case studies at various sites in Japan. In Proceedings of the 2nd International Conference on Microzonation for Safer Construction Research and Application, San Francisco, CA, USA, 26 November–1 December 1978; pp. 885–896.
76. Iwasaki, T.; Tokida, K.; Tatsuoka, F.; Watanabe, S.; Yasuda, S.; Sato, H. Microzonation for soil liquefaction potential using simplified methods. In Proceedings of the 3rd International Conference on Microzonation, Seattle, WA, USA, 28 June–1 July 1982; Volume 3, pp. 1319–1330.
77. Boulanger, R.W.; Idriss, I.M. *CPT and SPT Based Liquefaction Triggering Procedures*; Report No. UCD/CGM-14/01; Center for Geotechnical Modeling, Department of Civil and Environmental Engineering, University of California: Davis, CA, USA, 2014.
78. Robertson, P.K.; Wride, C.E. Evaluating cyclic liquefaction potential using the cone penetration test. *Can. Geotech. J.* **1998**, *35*, 442–459. [CrossRef]
79. Youd, T.L. Mapping of earthquake-induced liquefaction for seismic zonation. In Proceedings of the Fourth International Conference on Seismic Zonation, Stanford, CA, USA, 25–29 August 1991; Volume 1, pp. 111–147.
80. Hutabarat, D.; Bray, J.D. Estimating the severity of liquefaction ejecta using the cone penetration test. *J. Geotech. Geoenv. Eng.* **2022**, *148*, 04021195. [CrossRef]

81. Durap, A. Multi-decadal spatiotemporal shoreline vulnerability assessment (1987–2025): Integrating erosion-accretion dynamics for disaster risk reduction across 90 coastal transects. *Nat. Hazards* **2025**, *121*, 22981–23019. [CrossRef]
82. Durap, A. Beachface steepness modulates erosion but not recovery: Multi-decadal spatiotemporal shoreline evidence across 390 transects. *J. Sea Res.* **2025**, *208*, 102644. [CrossRef]

Disclaimer/Publisher's Note: The statements, opinions and data contained in all publications are solely those of the individual author(s) and contributor(s) and not of MDPI and/or the editor(s). MDPI and/or the editor(s) disclaim responsibility for any injury to people or property resulting from any ideas, methods, instructions or products referred to in the content.